



Detailed Description of the Collision Frequency in the Solar Atmosphere

Q. M. Wargnier^{1,2}, J. Martínez-Sykora^{1,2,3} , V. H. Hansteen^{1,2,3,4} , and B. De Pontieu^{1,3,4} ¹Lockheed Martin Solar & Astrophysics Laboratory, 3251 Hanover St., Palo Alto, CA 94304, USA²Bay Area Environmental Research Institute, NASA Research Park, Moffett Field, CA 94035, USA³Rosseland Centre for Solar Physics, University of Oslo, P.O. Box 1029 Blindern, NO0315 Oslo, Norway⁴Institute of Theoretical Astrophysics, University of Oslo, P.O. Box 1029 Blindern, N-0315 Oslo, Norway*Received 2022 February 15; revised 2022 May 5; accepted 2022 May 9; published 2022 July 14*

Abstract

This work aims to provide an accurate description and calculations of collision frequencies in conditions relevant to the solar atmosphere. To do so, we focus on the detailed description of the collision frequency in the solar atmosphere based on a classical formalism with Chapman–Cowling collision integrals, as described by Zhdanov. These collision integrals allow linking the macroscopic transport fluxes of multifluid models to the kinetic scales involved in the Boltzmann equations. In this context, the collision frequencies are computed accurately while being consistent at the kinetic level. We calculate the collision frequencies based on this formalism and compare them with approaches commonly used in the literature for conditions typical of the solar atmosphere. To calculate the collision frequencies, we focus on the collision integral data provided by Bruno et al., which is based on a multicomponent hydrogen–helium mixture used for conditions typical for the atmosphere of Jupiter. We perform a comparison with the classical formalism of Vranjes & Krstic and Leake & Linton. We highlight the differences obtained in the distribution of the cross sections as functions of the temperature. Then, we quantify the disparities obtained in numerical simulations of a 2.5D solar atmosphere by calculating collision frequencies and ambipolar diffusion. This strategy allows us to validate and assess the accuracy of these collision frequencies for conditions typical of the solar atmosphere.

Unified Astronomy Thesaurus concepts: [Solar chromosphere \(1479\)](#); [Collision processes \(2065\)](#)

1. Introduction

The solar chromosphere is a complex environment that is composed of many species where the ionization level, the temperature, and the collisional regime may vary by several orders of magnitude (see Vernazza et al. 1981). The chromosphere has transitions from a highly to a weakly collisional regime. In this region of the solar atmosphere, the species are coupled due to collisions and chemical interactions. The dynamics of each species depends on their respective collisional rates with other species. These collisional rates are altitude dependent because of the variation in densities and temperatures of each species (see Vranjes & Krstic 2013) under the assumption of semiempirical VAL-C models. However, this dependence becomes much more complex when the solar thermodynamics are taken into account, which could have orders-of-magnitude variation of the collision frequencies across the atmosphere (Martínez-Sykora et al. 2012). Therefore, an accurate description of these collisional effects is required to model the solar atmosphere accurately.

Several methods have been introduced in the literature to derive the collisional terms at the kinetic level. In the classical multifluid approaches considered for solar atmospheric conditions (see Leake et al. 2012; Alvarez Laguna et al. 2016; Ni & Lukin 2018; Popescu Braileanu et al. 2019; Ni et al. 2020; Wójcik et al. 2020; Niedziela et al. 2021; Pelekhatka et al. 2021), a simplification of the transport coefficients is usually considered. Indeed, the cross sections do not depend on the local thermodynamic condition of the plasma and are

sometimes assumed to be constant. Therefore, solid-sphere elastic collisions are assumed. However, at the kinetic level, the cross sections depend on the deflection angle and impact parameter describing binary collisions (see Woods 1995; Magin & Degrez 2004b; Zhdanov 2002). More specifically, the cross sections depend on the interaction potentials of the particles involved in a given collision. In this framework, the most accurate way to obtain the expression of the collisional terms is to derive them at the kinetic level, starting from the Boltzmann equation.

A well-known method to derive the transport properties at the kinetic level for multicomponent plasma is the Grads method (see Grad 1949; Zhdanov 2002). In this approach, irreducible tensorial Hermite polynomials are considered. The accuracy of the transport properties depends on the number of Hermite polynomials considered. In the literature, we are typically considering three main approximations: the 13N, 21N, and 29N moment approximations (see Zhdanov 2002; Struchtrup 2005). Alternatively, we have the spectral Galerkin method that is based on the Laguerre–Sonine polynomial approximation. This method has been described in detail by Kruger & Mitchner (1967) and Daybelge et al. (1968) to compute the transport properties for ionized gases in the presence of a magnetic field. In Ferziger & Kaper (1973) and Kolesnikov (2003), the computation has been extended to multicomponent plasma. In both approaches, the transport properties are dependent on collision integrals that link the macroscopic transport fluxes to the kinetic level, and they depend on the interaction potentials that govern the collisions (see Magin & Degrez 2004a, 2004b). However, none of these approaches have been considered to accurately calculate the collisional rates for solar atmospheric conditions.



Original content from this work may be used under the terms of the [Creative Commons Attribution 4.0 licence](#). Any further distribution of this work must maintain attribution to the author(s) and the title of the work, journal citation and DOI.

More recently, Vranjes & Krstic (2013) have provided a reliable quantitative set of data for collision frequencies, magnetization, viscosity, and thermal conductivity for the most important species in the solar atmosphere. The idea was to provide relevant data for any modeling of the solar atmosphere. However, in Vranjes & Krstic (2013), even though the data considered are known and haven been accepted as accurate by the scientific community, their interpretation to describe or calculate the collision frequencies in the solar atmosphere is not consistent with Grad’s method. Following the approaches of Ferziger & Kaper (1973), Kruger & Mitchner (1967), Kolesnikov (2003), and Zhdanov (2002), the collision frequencies depend only on the collision integrals, which are functions of the local thermodynamic conditions of the multicomponent plasma. In particular, to compute the collision integrals, an integration of the momentum transfer cross section over the energy is required. In Wargnier & et al. (2020), transport properties have been calculated in the context of a general hydrogen–helium mixture for solar atmospheric conditions. However, this approach is valid only for the multicomponent model developed by Graille et al. (2009). These calculations have not been performed yet in the context of multifluid magnetohydrodynamics (MHD) models (see Khomenko et al. 2014a, 2014b; Alvarez Laguna et al. 2016; González-Morales et al. 2018; Ni & Lukin 2018; Martínez-Sykora et al. 2019; Popescu Braileanu et al. 2019; Ni et al. 2020; Wójcik et al. 2020; Niedziela et al. 2021; Pelekhata et al. 2021) or single-fluid MHD models with an ambipolar diffusion coefficient that requires the calculation of collisional frequencies between ions and neutrals (see Nóbrega-Siverio et al. 2020).

This work aims to provide a reliable, accurate, and up-to-date set of data for modelers to calculate the collision frequencies in the context of solar physics. Based on the formalism of Zhdanov (2002), which follows the Grad method, we apply the definition of the collision frequencies involved in the 13N moment model. In this formalism, the collision frequencies depend on collision integrals to be consistent at the kinetic level (see Kruger & Mitchner 1967). We consider a hydrogen–helium-ionized metals mixture to be representative of solar atmospheric conditions. The data associated with collision integrals have been taken from a library named *Mutation++* (see Magin & Degrez 2004b; Scoggins et al. 2016), originally taken from Bruno et al. (2010). Based on a review of the literature, Bruno et al. (2010) have provided collision integrals as a function of the temperature for a general hydrogen–helium mixture under Jovian atmosphere conditions. Concerning interactions involving ionized metals, we consider the approach of Oppenheim et al. (2020), who consider these collisions as classical Maxwell molecular collisions. We compute the cross sections and collision frequencies for all the interactions involved in the mixture in a 2.5D simulation of the solar atmosphere from the photosphere to the corona performed with *Bifrost* (Gudiksen et al. 2011; Martínez-Sykora et al. 2018; Martínez-Sykora et al. 2019). This model has been built from a resistive single-fluid MHD model with ambipolar diffusion (See Section 4.2). We compare collision frequencies calculated with the formalism based on collision integrals with the formalism of Vranjes & Krstic (2013) and Leake et al. (2012) and assess the differences between the two approaches for solar atmospheric conditions. We also focus on the ambipolar diffusion coefficient in the context of a single-fluid approach to take into account ion–

neutral interactions (see Martínez-Sykora et al. 2019; Nóbrega-Siverio et al. 2020). Two different approaches to calculate the ambipolar diffusion coefficients are considered: a classical approach based on the data from Vranjes & Krstic (2013), and an approach based on collision integrals from Zhdanov (2002). The whole strategy of this work highlights the possible impact of the collision integral formalism on understanding the dynamics of the solar atmosphere.

The structure of the paper is as follows. In Section 2 we present the mixture considered and some notation. In Section 3 we provide a brief overview the derivation of the 13N moment model using the Grad method as introduced by Zhdanov (2002), the definition of the momentum and energy exchange terms, as well as the collision frequencies based on a formalism involving collision integrals. In Section 4 we compare the formalism introduced in the 13N moment model (see Zhdanov 2002) based on the data provided by Bruno et al. (2010) with Vranjes & Krstic (2013) and Leake & Linton (2013) by focusing on the cross sections. We highlight and quantify the differences obtained between the three approaches for each interaction involved in the mixture considered. Additionally, we also compare the three approaches in a 2.5D simulations of the solar atmosphere (from the photosphere to the corona) with *Bifrost* by calculating both the cross sections and collision frequencies. In Section 5 we investigate the impact of each approach on the ambipolar diffusion term considered in the generalized Ohm law, which takes into account ion–neutral interactions.

2. Mixture and Notation

We focus on a hydrogen–helium-ionized metal mixture (for which we include the most abundant species in the solar atmosphere), defined by

$$\mathfrak{M} = \{\text{H}, \text{H}^+, \text{He}, \text{He}^+, \text{He}^{++}, \text{Ne}^+, \text{Fe}^+, \text{Mg}^+, \text{Ni}^+, \text{O}^+, \epsilon\}, \quad (1)$$

where ϵ denotes the electrons. For the sake of simplicity, no excited levels are considered in this work. However, we point out that the strategy and theory described in this study can be generalized to any multicomponent plasma mixtures when the collision integrals or interaction potentials for each interaction are provided. Therefore, it is possible to extend this strategy to any mixture or consider different species for conditions different from those in the solar atmosphere.

For clarity and consistency, we use the same nomenclature as was used by Martínez-Sykora et al. (2019), Ballester et al. (2018), and Khomenko et al. (2014a) with minor adjustments. The ionization states are referred to as \mathcal{J} , i.e., $\mathcal{J} = 0$ denotes neutrals and $\mathcal{J} \geq 1$ denotes ions. The identity of the chemical species is indicated by α . Consequently, each set of particles in a given microstate is described with $\alpha\mathcal{J}$. For electrons, the notation $\alpha\mathcal{J}$ is reduced to just ϵ . For simplicity, \sum_{α} is the sum over all the species α , and $\sum_{\mathcal{J},\alpha}$ is the sum over all ionization levels, including neutrals, for a given species α . For clarity, we define $\sum_{\alpha\mathcal{J}} = \sum_{\alpha} \sum_{\mathcal{J},\alpha}$.

3. Definition of the Collision Frequency

First, we introduce the description of the momentum and energy exchange terms due to collisions, consistent with

the 13N moment model derived from Grad's method (see Grad 1949; Zhdanov 2002). This approach is valid for any multicomponent plasma mixture in thermal nonequilibrium. Then, we provide the definition of the corresponding collision frequency based on a formalism with collision integrals.

3.1. Derivation of the Momentum and Energy Exchange Terms

In order to obtain the 13N moment model, each distribution function associated with one type of particle is expanded in series of tensorial Hermite polynomials in order to approximate the solution of the Boltzmann equations. Each distribution function denoted by $f_{a\tilde{J}}$, $a\tilde{J} \in \mathfrak{M}$ is assumed to be a perturbation of a local Maxwellian distribution function at its respective temperature $T_{a\tilde{J}}$. The local Maxwellian is naturally chosen as the zero approximation of the distribution function. Then, by first using the expressions of the first few Hermite polynomials, which lead to expansion coefficients that are related to macroscopic quantities of clear physical meaning, and second, by expanding the distribution function, we finally obtain a closed system of equations, called the 13N moment model. The system of equations includes equations for the densities, momentum, and internal energies for each particle $a\tilde{J} \in \mathfrak{M}$, as well as equations for the transport quantities, such as viscous stress tensors, reduced heat fluxes, and diffusion velocities. Note that on the right-hand side of the transport equations, we obtain the moments with respect to the collision integrals. These terms are the momentum and energy transfer terms due to collisions and allow defining the collision frequency through the formalism with Chapman–Cowling collision integrals.

In the context of the 13N moment formulation (see Chapter 4, Equation (4).2.16 from Zhdanov 2002), each momentum equation associated with a particle $a\tilde{J} \in \mathfrak{M}$, the momentum exchange term between particles with a given microstate $a\tilde{J} \in \mathfrak{M}$ and particles with another microstate $a'\tilde{J}' \in \mathfrak{M}$ with $a\tilde{J} \neq a'\tilde{J}'$, is defined as

$$\mathbf{R}_{a\tilde{J}}^{a\tilde{J},a'\tilde{J}'} = m_{a\tilde{J}} n_{a\tilde{J}} \nu_{a\tilde{J},a'\tilde{J}'}^{\text{col}} (\mathbf{u}_{a'\tilde{J}'} - \mathbf{u}_{a\tilde{J}}), \quad (2)$$

where $\mathbf{u}_{a\tilde{J}}$ and $\mathbf{u}_{a'\tilde{J}'}$ are the velocity of species $a\tilde{J}$ and $a'\tilde{J}'$, respectively, $\nu_{a\tilde{J},a'\tilde{J}'}^{\text{col}}$ is the collision frequency between particles $a\tilde{J}$ and $a'\tilde{J}'$, and $n_{a\tilde{J}}$ and $m_{a\tilde{J}}$ are the density number and the mass of particle $a\tilde{J}$. Additionally, ignoring terms that involve the heat fluxes, each equation of internal energy associated with a particle $a\tilde{J} \in \mathfrak{M}$, we have the energy exchange term defined as

$$Q_{a\tilde{J}}^{a\tilde{J},a'\tilde{J}'} = \nu_{a\tilde{J},a'\tilde{J}'}^{\text{col}} m_{a\tilde{J},a'\tilde{J}'} n_{a\tilde{J}} |\mathbf{u}_{a'\tilde{J}'} - \mathbf{u}_{a\tilde{J}}|^2 + \nu_{a\tilde{J},a'\tilde{J}'}^{\text{col}} \left(\frac{3m_{a\tilde{J}}}{m_{a\tilde{J}} + m_{a'\tilde{J}'}} \right) n_{a\tilde{J}} k_B (T_{a'\tilde{J}'} - T_{a\tilde{J}}), \quad (3)$$

where the reduced mass is defined as $m_{a\tilde{J},a'\tilde{J}'} = m_{a\tilde{J}} m_{a'\tilde{J}'} / (m_{a\tilde{J}} + m_{a'\tilde{J}'})$, k_B is the Boltzmann constant, and $T_{a'\tilde{J}'}$ and $T_{a\tilde{J}}$ are the temperatures of species $a'\tilde{J}'$ and $a\tilde{J}$, respectively. In Equation (3), the first component corresponds to the heating produced by the velocity drift between species $a\tilde{J}$ and $a'\tilde{J}'$ due to collisions. The second component corresponds to a term associated with the relaxation of the temperature $T_{a\tilde{J}}$ toward $T_{a'\tilde{J}'}$ at a collisional rate $\nu_{a\tilde{J},a'\tilde{J}'}^{\text{col}}$. Both components have a characteristic timescale equal to the collision timescale between $a\tilde{J}$ and $a'\tilde{J}'$. Note that the presented terms are valid only in the

framework of the 13N moment formulation. Different source terms in energy or momentum equations can be found in the literature (see Wargnier & et al. 2020).

3.2. Description of the Collision Frequency

The collision frequency involved in Equations (2) and (3) is defined as

$$\nu_{a\tilde{J},a'\tilde{J}'}^{\text{col}} = \frac{4}{3} \frac{m_{a\tilde{J},a'\tilde{J}'}}{m_{a\tilde{J}}} n_{a'\tilde{J}'} |\mathbf{u}_{a\tilde{J},a'\tilde{J}'}^{\text{th}}| \Omega_{a\tilde{J},a'\tilde{J}'}^{1,1} \quad (4)$$

where $|\mathbf{u}_{a\tilde{J},a'\tilde{J}'}^{\text{th}}|$ is the mean thermal speed between particles $a\tilde{J}$ and $a'\tilde{J}'$, and $\Omega_{a\tilde{J},a'\tilde{J}'}^{1,1}$ is the generalized well-known Chapman–Cowling collision integral (see Chapman & Cowling 1970). In this study, we focus only on the first terms of the expansion corresponding to the 13N moment approach. However, it is important to note that, if a higher-order approximation of the distribution function is considered, the expression presented in Equation (4) would involve additional collision integrals of higher orders. Further details are given in Magin & Degrez (2004a, 2004b), Graille et al. (2009), and Wargnier & et al. (2020).

The mean thermal speed between particles $a\tilde{J}$ and $a'\tilde{J}'$ is defined as

$$|\mathbf{u}_{a\tilde{J},a'\tilde{J}'}^{\text{th}}| = \sqrt{\frac{8}{\pi \mu_{a\tilde{J},a'\tilde{J}'}}}, \quad (5)$$

where

$$\mu_{a\tilde{J},a'\tilde{J}'} = \frac{\mu_{a\tilde{J}} \mu_{a'\tilde{J}'}}{\mu_{a\tilde{J}} + \mu_{a'\tilde{J}'}} \quad \mu_{a\tilde{J}} = \frac{m_{a\tilde{J}}}{k_B T_{a\tilde{J}}}, \quad a\tilde{J}, a'\tilde{J}' \in \mathfrak{M}^2. \quad (6)$$

The generalized Chapman–Cowling collision integral (see Chapman & Cowling 1970) is defined as

$$\Omega_{a\tilde{J},a'\tilde{J}'}^{(l,s)} = \frac{4(l+1)}{(s+1)! [2l+1 - (-1)^l]} \mathbb{G}^{(l)}(\mu_{a\tilde{J},a'\tilde{J}'}), \quad (7)$$

where superscripts l and s are related to the Laguerre–Sonine polynomials of the spectral method, and

$$\mathbb{G}^{(l)}(\mu_{a\tilde{J},a'\tilde{J}'}) = \int_0^\infty \exp(-g^2) g^{2s+3} \mathfrak{Q}_{a\tilde{J},a'\tilde{J}'}^{(l)} d\mathbf{g}. \quad (8)$$

Note that, excluding charged interactions, collision integrals defined in Equation (7) depend solely on temperature. In Equation (8), $\mathfrak{Q}_{a\tilde{J},a'\tilde{J}'}^{(l)}$ is the transport cross section, and the reduced collision velocity \mathbf{g} is defined as

$$\mathbf{g} = \sqrt{\frac{\mu_{a\tilde{J},a'\tilde{J}'}}{2}} \mathbf{g}, \quad (9)$$

with \mathbf{g} the relative velocity between particle $a\tilde{J}$ and $a'\tilde{J}'$. Following the definition of Bruno et al. (2010), Magin & Degrez (2004b), Ferziger & Kaper (1973), and Woods (1995), the transport cross section is defined as

$$\begin{aligned} \mathfrak{Q}_{a\tilde{J},a'\tilde{J}'}^{(l)} &= 2\pi \int_0^\infty [1 - \cos^l(\chi)] b db \\ &= 2\pi \int_0^\pi [1 - \cos^l(\chi)] \sigma \sin(\chi) d\chi, \end{aligned} \quad (10)$$

where $b = b_{a\tilde{J},a'\tilde{J}'}$ is the impact parameter, $\sigma = \sigma(\mathbf{g}, \chi_{a\tilde{J},a'\tilde{J}'})$ is the elastic collision differential cross section, and

$\chi = \chi_{\alpha\bar{J},\alpha'\bar{J}'}$ is the deflection angle between particles $\alpha\bar{J}$ and $\alpha'\bar{J}'$. Note that if $l = 1$ in Equation (10), we obtain the so-called momentum transport cross section. If $l = 2$, we obtain the so-called viscous transport cross section. In classical mechanics, the deflection angle χ is related to a given interaction potential ϕ as follows:

$$\chi = \pi - 2b \int_{r_m}^{\infty} \frac{dr/r^2}{\sqrt{1 - b^2/r^2 - \phi(r)/E_{\alpha\bar{J},\alpha'\bar{J}'}}}, \quad (11)$$

where r is the distance between the two colliding particles $\alpha\bar{J}$ and $\alpha'\bar{J}'$, r_m is the distance of the closest approach, and $E_{\alpha\bar{J},\alpha'\bar{J}'} = m_{\alpha\bar{J},\alpha'\bar{J}'}|\mathbf{g}|^2/2$ is the kinetic energy associated with the relative velocity \mathbf{g} . $\phi = \phi_{\alpha\bar{J},\alpha'\bar{J}'}$ is the phenomenological potential that simulates the average interaction between the two colliding particles $\alpha\bar{J}$ and $\alpha'\bar{J}'$, allowing the direct evaluation of collision integrals for unknown collisional systems.

3.3. Calculation of Collision Integrals

Most of the phenomenological interaction potentials used to describe the interactions involved in the mixture \mathfrak{M} are those described by Bruno et al. (2010). The interaction potentials have been fitted with several analytical forms such as the Hulbert–Hirschfelder potential (see Rainwater et al. 1982), the modified Morse potential (see Kuntz & Roach 1972), the modified repulsive potential (see Aubreton et al. 2003), the inverse power potential (see Kihara et al. 1960), or other phenomenological potentials described by Pirani et al. (2004, 2006). Note that concerning interactions that involve ionized metals, the interaction potential function follows a polarization model, as described by Bruno et al. (2010) and Oppenheim et al. (2020). Further details are given in Appendix B. For charged-particle interactions, we refer to Appendix A.

In summary, in order to calculate the collision frequency defined in Equation (4), it is necessary to first compute the collision integral $\Omega^{(l,1)}$ defined in Equation (8). This collision integral is computed from the integration over the reduced collision velocity \mathbf{g} of the momentum transport cross section $\Omega^{(l)}$ defined in Equation (10). Then, the momentum transport cross section is the result of the integration of the elastic differential cross section σ with respect to the impact parameter b or deflection angle χ defined in Equation (11). Finally, the deflection angle can be determined by the integration of a given interaction potential that mimics the interaction between two particles, as presented in Equation (11).

In the literature, data from experimental measurements are provided to calculate the collision integrals. Generally, these data are based on

1. the measured transport cross section $\Omega_{\alpha\bar{J},\alpha'\bar{J}'}^{(l)}$ as a function of the relative kinetic energy $E_{\alpha\bar{J},\alpha'\bar{J}'}$ (called the momentum ($l = 1$), viscous ($l = 2$), or elastic scattering cross sections),
2. or on the measured elastic collision differential cross section σ as a function of the deflection angle χ ,
3. or on a measured interaction potential fitted with a phenomenological potential ϕ to analytically compute the deflection angle χ , which allows calculating the transport cross section $\Omega_{\alpha\bar{J},\alpha'\bar{J}'}^{(l)}$.

In the case of the mixture \mathfrak{M} , the preferred method to calculate collision integrals is the numerical integration of accurate ab initio phenomenological interaction potentials as performed by Bruno et al. (2010).

4. Comparison with Classical Approaches in Solar Physics

In Bruno et al. (2010), a complex mixture composed of {He, He⁺, He⁺⁺, H, H⁺, H⁻, H₂, H₂⁺, e} has been considered to compute some collision integrals for Jovian atmospheric conditions for a range of temperatures from 50 to 50,000 K. We point out that the collision integral data considered for the Jovian atmosphere can be applied to any other environments (such as the solar atmosphere) for any range of densities and temperatures as long as the continuum description of the multicomponent plasma is valid. In this work, we assume that the continuum description is valid from the photosphere to the corona. However, this assumption can be reconsidered at larger scales.

In this study, we focus on the mixture \mathfrak{M} , which includes some of the species considered by Bruno et al. (2010). The following subsections review interaction potential functions for each type of interaction involved in \mathfrak{M} and exhibit the data sources required to calculate the collision integrals. For the sake of clarity, in the following sections, the approach based on the 13N moment approach with a formalism of collision integrals based on the data provided by Bruno et al. (2010) is denoted as approach [1] (hereafter [A1]). The collision frequency defined in Equation (4) is denoted by $\nu_{\alpha\bar{J},\alpha'\bar{J}'}^{\text{col},[1]}$. In addition, we compare this approach with the approach from Vranjes & Krstic (2013) and Vranjes et al. (2008), denoted as approach [2] (hereafter [A2]), which have been extensively used (e.g., Khomenko et al. 2018; Martínez-Sykora et al. 2019), and Leake & Linton (2013), denoted as approach [3] (hereafter [A3]).

In both [A2] and [A3], the collision frequency between particles with a given microstate $\alpha\bar{J} \in \mathfrak{M}$ and particles with another microstate $\alpha'\bar{J}' \in \mathfrak{M}$, where $\alpha\bar{J} \neq \alpha'\bar{J}'$ can be described by

$$\nu_{\alpha\bar{J},\alpha'\bar{J}'}^{\text{col},[2,3]} = \frac{m_{\alpha\bar{J},\alpha'\bar{J}'}}{m_{\alpha'\bar{J}'}} n_{\alpha'\bar{J}'} |\mathbf{u}_{\alpha\bar{J},\alpha'\bar{J}'}^{\text{th}}| C_{\alpha\bar{J},\alpha'\bar{J}'}(T_{\alpha\bar{J},\alpha'\bar{J}'}), \quad (12)$$

where the mixed temperature is defined as $T_{\alpha\bar{J},\alpha'\bar{J}'} = (m_{\alpha\bar{J}}T_{\alpha\bar{J}} + m_{\alpha'\bar{J}'}T_{\alpha'\bar{J}'})/(m_{\alpha\bar{J}} + m_{\alpha'\bar{J}'})$ and $C_{\alpha\bar{J},\alpha'\bar{J}'}$ is the so-called cross section between particles $\alpha\bar{J}$ and $\alpha'\bar{J}'$. In the following, for some of the interactions, we compare the cross sections $C_{\alpha\bar{J},\alpha'\bar{J}'}$ (for both [A2] and [A3]) with its equivalent in the formula presented in Equation (4) ([A1]), i.e., with the coefficient $4/3 \Omega_{\alpha\bar{J},\alpha'\bar{J}'}^{1,1}$ as a function of the temperature. For the sake of simplicity, we assume that the mean relative speed, the number densities of each species, and temperature are identical for all the approaches considered. Thus, only the cross sections as a function of the temperature differ between [A1], [A2], and [A3]. Note that to compute the number density of each species, we have assumed photospheric abundances, and the ionization fraction has been calculated assuming Saha-Boltzmann.

Note that in [A1], for temperatures above 5×10^4 K, the collision integrals have been extrapolated up to 4×10^5 K using the fitting expressions provided by Bruno et al. (2010). We point out that this extrapolation at higher temperature is the most convenient current approach as most of the data for the cross sections have been validated only at lower temperatures.

Table 1
Electron–Neutral and Neutral–Neutral Interaction Data for Cross Sections for Approaches [1] and [2].

Type	Pairs	Approach [1]: Collision Integral $\Omega^{1,1}$	Approach [2]: C
Electron–neutral	ϵ –H	Integration of the differential cross sections from Bray et al. (1991), Gupta & Mathur (1980), Gorse & Capitelli (2001), and Alves et al. (2013).	The data of cross sections are calculated as some mean values from Bederson & Kieffer (1971).
	ϵ –He	Identical approach as in the ϵ –H interaction.	Identical approach as in the ϵ –H interaction.
Neutral–neutral	H–H	Collision integral data from Stallcop et al. (1996, 1998).	Momentum transfer cross sections from Krstic & Schultz (1998, 1999).
	He–He	Integration of the interaction potential from Hurly & Mehl (2007).	N/A
	H–He	Integration of a Hulburt–Hirschfelder potential to fit the experimental interaction potentials provided by Olson & Liu (1980), Li & Lin (2009).	N/A

For temperatures above 4×10^5 K, the collision integrals are assumed to be constant. This assumption has been considered in order to avoid discontinuities in the collision frequencies. In [A2], data for the cross sections (in particular, Krstic & Schultz 1998, 1999) are provided for a maximum energy equal to 100 eV, which corresponds to approximately 10^6 K. Above these temperatures, the cross sections are assumed to be constant. Note that the values of the collision integrals or cross sections at these high temperatures are not really important as it coincides with a collisionless plasma where the density is very low. In this context, the continuum description of the plasma is not valid, and collision frequencies are negligible.

Note that from a theoretical point of view, the difference between approaches [A1] and [A3] is essentially due to the fact that in [A3], a constant cross section that does not depend on temperature has been considered. This approximation has been used by Leake & Linton (2013; and also by other previous studies, e.g., Martínez-Sykora et al. 2012; Khomenko & Collados 2012) for the purpose of modeling a magnetic reconnection event in lower chromosphere conditions, i.e., for conditions where the average temperature does not vary by several orders of magnitude, as is the case in the solar atmosphere. Even though identical or similar transport cross section data have been considered (e.g., Krstic & Schultz 1999, 1998), the main difference between approaches [A1] and [A2] is that the cross section C involved in Equation (12) has been defined as being either the momentum transport cross section Ω^1 or the sum of the elastic scattering and charge-exchange cross sections for ion–neutral interactions. Therefore, in [A2], the approach is not consistent with the 13N moment model because the collision integrals are not calculated at all, and the momentum transport cross section has not been integrated as it is required in the formalism of [A1] presented in Equation (7). This difference in approach leads to significant differences in the calculated collision frequencies, as we show below.

4.1. List of Interactions

In the mixture \mathfrak{M} , several types of interactions are involved. Data to calculate the cross sections and collision integrals are shown in Tables 1 and 2. In summary, we have

1. Electron–neutral interactions, such as ϵ –H and ϵ –He interactions,
2. Neutral–neutral interactions, such as H–H, H–He, or He–He interactions,
3. Ion–neutral interactions, which can be subdivided into
 - (a) Interactions involving resonant charge transfer, such as He–He⁺, H–H⁺, and He–He⁺⁺.

- (b) Interactions involving metals such as α -Fe⁺, α -Mg⁺, α -O⁺, and α -Ne⁺ for $\alpha \in \{\text{H, He}\}$. Note that these interactions can be seen as classical Maxwell molecular collisions, as presented by Oppenheim et al. (2020).

- (c) Other ion–neutral interactions, such as He–H⁺, H–He⁺, and H–He⁺⁺.

4. Charged or Coulomb interactions, which involve all the possible combinations of interactions between ionized species such as He⁺, He⁺⁺, ϵ , H⁺, Fe⁺, Mg⁺, O⁺, and Ne⁺. These interactions have been widely studied in the literature (see Spitzer 1963; Capitelli et al. 2000), thus, they are not the main focus of this work. Further details are given in Appendix A.

No data for the cross sections associated with the He–H, He–He, He–He⁺, H–He⁺, H–He⁺⁺, and He–He⁺⁺ interactions have been provided by Vranjes & Krstic (2013). Therefore, no comparison between [A1] and [A2] are performed for these interactions. However, we present the temperature dependence of these cross sections.

4.2. Model of the Solar Atmosphere

For a better understanding of the differences of the various approaches, we compare them using the 2.5D radiative MHD numerical simulation (so-called GOL) described in detail in Martínez-Sykora et al. (2017a, 2017b). The simulation has been calculated with the 3D radiative MHD *Bifrost* code (Gudiksen et al. 2011) with scattering (Hayek et al. 2010; Carlsson & Leenaarts 2012). This model includes type I and II spicules. It provides a better understanding of the parameter range of the collisional rates for the various approaches [A1], [A2], and [A3] for the solar atmosphere than 1D semiempirical models.

The simulated solar atmosphere spans 90 Mm horizontally and from 3 Mm below to 40 Mm above the surface. The magnetic field configuration includes two plage regions of opposite polarities where the average magnitude is ~ 190 G. Loops that are up to 50 Mm long connect the two opposite polarities. The boundary conditions are periodic in the horizontal direction and open in the vertical direction. The current work focuses on a restricted domain from 12.5 Mm to 18 Mm in the horizontal direction and from 0 to 10 Mm in the vertical direction, containing relevant chromospheric features of the simulation, e.g., spicules, magneto-acoustic shocks, and cold bubbles. This region encompasses the photosphere, chromosphere, transition region, and corona. The horizontal resolution is uniform with a 14 km grid spacing, while the vertical resolution is nonuniform, with the highest resolution in

Table 2
Ion–Neutral Interaction Data for Cross Sections for Approaches [1] and [2]

Type	Pairs	Approach [1]: Collision Integral $\Omega^{l=1}$	Approach [2]: C
Resonant charge transfer	He–He ⁺	Integration of a Hulbert–Hirschfelder potential combined with a modified repulsive potential to fit the potential of Aubreton et al. (2003). The charge-exchange collision integrals associated with this interaction have been fitted from the data provided by Rundel et al. (1979).	N/A
	H–H ⁺	Integration of the momentum and charge-exchange transfer cross sections from Krstic & Schultz (1999, 1998).	Sum of the elastic scattering and charge-exchange transfer cross section from Krstic & Schultz (1999, 1998).
	He–He ⁺⁺	The elastic contribution is based on the integration of an interaction potential based on a polarization model. The charge-exchange contribution has been fitted from Janev et al. (1987).	N/A
Maxwell molecular collisions	α -ionized metals, $\alpha \in \{H, He\}$	Integration of an interaction potential that follows a polarization model where the polarizability coefficients of all species have been taken from Schwerdtfeger & Nagle (2019).	Formula based on the ratio of mass between neutrals and metals based on Vranjes et al. (2008).
Others	He–H ⁺	Integration from the data provided by Krstic & Schultz (1999, 1998) in the frame of a quantum approach in the range of [0.1, 100] eV. For lower energy ranges ($E < 0.1$ eV), a polarization model has been considered.	Momentum transfer cross sections from Krstic & Schultz (1999, 1998).
	H–He ⁺	Integration of a Hulbert–Hirschfelder potential to fit the ab initio potential of Aubreton et al. (2003).	N/A
	H–He ⁺⁺	Integration of an interaction potential based on a polarization model.	N/A

the photosphere, chromosphere, and transition region (12 km grid spacing). Further details about the setup can be found in Martínez-Sykora et al. (2017a).

4.3. Electron–Neutral Interactions

In [A2], in order to compute the collision frequency provided in Equation (12), the cross section C has been considered as being equal to the momentum transfer cross section $\Omega^{(l=1)}$ provided by Bederson & Kieffer (1971), i.e., $C_{\epsilon-H} = \Omega_{\epsilon-H}^1$ and $C_{\epsilon-He} = \Omega_{\epsilon-He}^1$. In [A3], a constant cross section $C_{\epsilon-H} = C_{\epsilon-He} = 10^{-15} \text{ cm}^2$ has been used for both interactions.

In Figure 1 we compare the cross sections in cm^2 as a function of the temperature in kelvin based on [A1], [A2], and [A3]. We compare the cross sections associated with the ϵ –He (top), and ϵ –H (bottom) interactions. From 10^3 K to 10^4 K, the cross section associated with the ϵ –He interaction is higher in [A1] than in [A2]. For a higher temperature, in [A1] the cross section is decreasing drastically, whereas in [A2] it is approximately constant at $6 \times 10^{-16} \text{ cm}^2$. In the bottom row of Figure 1, for temperatures below 5×10^3 K, the cross sections associated with the ϵ –H interaction are higher in [A1] than in [A2]. For temperatures higher than 5×10^3 , the cross section is higher in [A2] than in [A1].

In Figure 2 we compare the distribution of the cross sections based on approaches [A1] and [A2] in the 2.5D simulation of the solar atmosphere described in Section 4.2. Several regions of the simulated solar atmosphere can be identified and characterized based on the different altitude, range of total mass density, and temperature:

1. from $z = 0$ Mm to $z = 0.8$ Mm, we can identify the photosphere where the temperature ranges around several thousand kelvin and the total mass density decreases from 10^{-8} to $10^{-10} \text{ g cm}^{-3}$, denoted by region [A],

2. from $z = 0.8$ Mm to approximately $z = 2$ Mm, we have the lower-mid chromosphere where the temperature increases from several thousand kelvin to 10^4 K and the total mass density decreases from 10^{-10} to $10^{-12} \text{ g cm}^{-3}$, denoted as region [B],
3. from $x = 14$ to $x = 16$ Mm and from $z = 2$ to $z = 5$ Mm, we have a spicule that encompasses the upper chromosphere and transition region, where the temperature increases from 10^4 K to more than 10^5 K and the total mass density decreases from 10^{-12} to $10^{-14} \text{ g cm}^{-3}$, denoted as region [C],
4. for any $z > 5$ Mm, we have the upper transition region and solar corona, where the temperature increases from 10^5 to 10^6 K and the total mass density decreases from $10^{-14} \text{ g cm}^{-3}$ to lower than $10^{-15} \text{ g cm}^{-3}$, denoted as region [D],

Note the presence of type II spicules, which permeate from the chromosphere $z > 2$ Mm into the transition region and corona.

The cross section associated with the ϵ –He (panels (A)–(E)) interaction based on [A1] is higher than in [A2] at $T < 10^4$ K, but is negligible at higher temperatures. From region [A] to region [B], the cross sections are approximately constant for [A1] and [A2] because the temperature ranges from 10^3 K to 10^4 K. In region [C], at the border of the spicule, the cross sections decrease drastically for [A1] and [A2] due to the large increase of the temperature in the transition region. In the bottom row of Figures 2(F)–(J), for both approaches, the cross sections associated with the ϵ –H interaction decrease from region [A] to region [D] as they are decreasing functions of the temperature according to Figure 1. From region [A] to region [B], the cross sections are higher in [A1] than in [A2] because $T < 10^4$ K. However, from region [C] to region [D], the cross sections are higher in [A2] than in [A1] as the temperature is higher than 10^4 K.

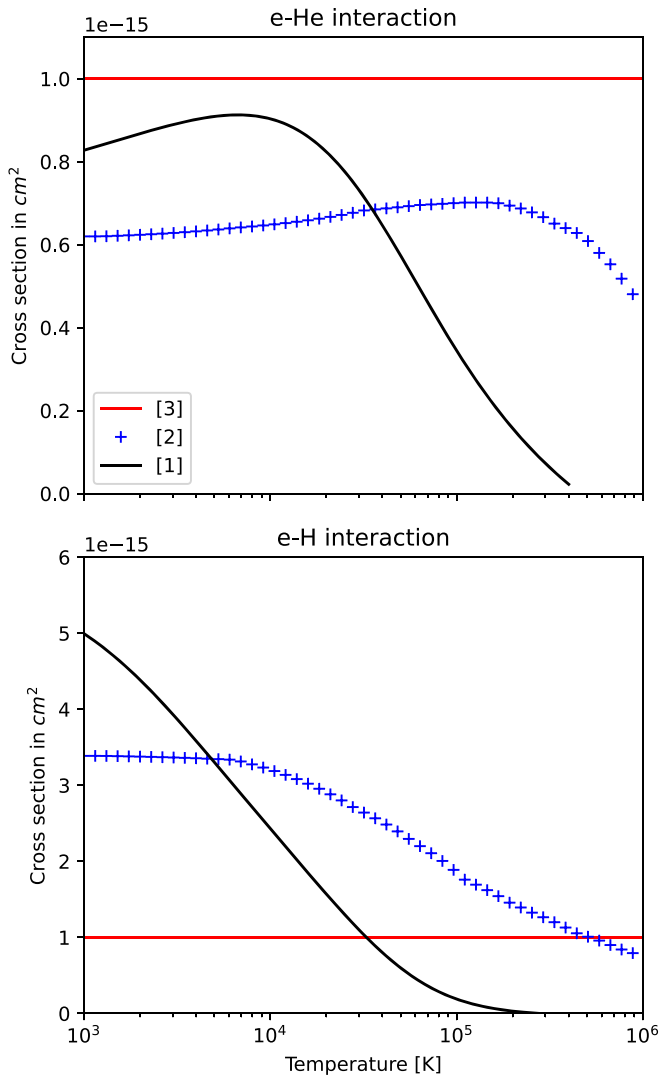


Figure 1. Variation in the cross section (in cm^2) as a function of the temperature (in kelvin). The full red and black lines correspond to the cross section of [A3] (i.e., $C_{e,a\mathcal{J}}(T)$, $a\mathcal{J} \in \{\text{H}, \text{He}\}$ from Equation (12)) and [A1] based on the formalism introduced in Equation (4) (i.e., $4/3 \Omega_{e,a\mathcal{J}}^{1,1}(T)$, $a\mathcal{J} \in \{\text{H}, \text{He}\}$), respectively, the blue line with crosses corresponds to the cross section used in [A2] (i.e., $C_{e,a\mathcal{J}}(T) = 10^{-15} \text{ cm}^2$, $a\mathcal{J} \in \{\text{H}, \text{He}\}$ from Equation (12)). From top to bottom: ϵ -He and ϵ -H interaction.

Concerning the ϵ -He interaction (Figure 2(D)), the ratio of the cross sections between the two approaches is around 0.75 from regions [A] to [C]. These results are consistent with Figure 1, where for temperatures below 10^4 K, the ratio of the two approaches corresponds to approximately $0.8/0.6 \approx 0.75$. In region [D], the ratio increases drastically as the cross section is negligible for [A1] and not for [A2], as presented in Figure 1. Concerning the ϵ -H interaction (Figure 2(I)), the ratio oscillates between 0.8 and 1 from the convection zone to the bottom of the chromosphere, whereas from the bottom of the chromosphere to the transition region, the ratio ranges from 1.0 to 1.2. This distribution can easily be explained with the 1D distributions presented at the bottom of Figure 1. Below 5×10^3 K, [A1] is slightly higher than [A2], leading to a ratio slightly lower than 1 at these temperatures, corresponding to regions [A] and [B]. For a higher temperature, corresponding to the region [C], [A1] is slightly lower than [A2], leading to a ratio higher than 1.

Figures 3(A) and (B) show similar distributions between [A1] and [A2]. From region [A] to [B], the collision frequency decreases from 10^7 s^{-1} to $10^{3.5} \text{ s}^{-1}$. In region [C], the collision frequency decreases from $10^{3.5}$ to 1 s^{-1} . Finally, in region [D], the collision frequency is negligible because the density of helium is negligible (panel (A)). Note that the ratios of the collision frequencies presented in Figures 3(D) and (I) are identical to the ratios of cross sections presented in Figures 2(D) and (I) as we assume that the temperature and number densities of all species are identical between approaches [A1] and [A2]. The only difference is in region [D], where the ratio is null in Figure 3, but is constant in Figure 2. This is due to the fact that the number densities of neutral helium and hydrogen are null in this region, leading to a singularity in the ratio of the collision frequencies. To remove this singularity, a null ratio has been assumed in this region.

As for the distribution of the neutral helium (Figure 3(A)), the number density of neutral hydrogen (panel (F)) decreases from region [A] to region [D], leading to a decrease of the collision frequency between electrons and neutral hydrogen. For further details about the magnitude of the collisional frequencies between electrons and neutral hydrogen and the ratio of the two approaches, we refer to Figures 3(F)–(I).

4.4. Neutral–Neutral Interactions

In this subsection, we focus on the H–H, H–He, and He–He interactions. Note that in [A3], a constant cross section $C = 7.73 \times 10^{-15} \text{ cm}^2$ has been used for all neutral–neutral interactions.

In the top panel of Figure 4, we focus on the H–H interaction. In the bottom panel, we show the cross sections associated with the He–H and He–He interaction based on [A1]. In the top panel of Figure 4, the cross section associated with the H–H interaction is a decreasing function of the temperature in both approaches [A1] and [A2]. However, in [A2], the cross section is much larger than in [A1] by at least one order of magnitude. At high temperatures $T > 10^5$ K, the cross section is negligible in [A1]. Note that in [A2] small oscillations in the cross section have been obtained at lower temperature, associated with resonant quantum effects (Vranjes & Krstic 2013). These effects are not obtained in [A1] because of the integration of the momentum transport cross section with respect to the energy, which smoothes the distribution.

In Figure 5 we show that the cross section in [A2] is larger than in [A1] by at least one order of magnitude within the chromosphere. In approaches [A1] and [A2], we obtain a large decrease in the cross sections in the transition region. Similarly as in Figure 2, in region [D], the cross section is negligible in [A1], but it reaches a minimum of 10^{-14} cm^2 for [A2]. In summary, the ratio associated with the H–H cross section ranges between 10 and 15 from regions [A] to [C]. Similarly as in the previous section, the distribution of the ratio in panel (C) from Figure 5 can be explained from Figure 4. Indeed, at the top of Figure 4, for all the considered range of temperature, the difference between the two cross sections is about one order of magnitude. Therefore, for all the regions considered, the ratio between approaches [A1] and [A2] ranges from 10 to 20.

In Figure 6 we focus on the distribution of the logarithm of the collision frequencies associated with H–H interaction. As

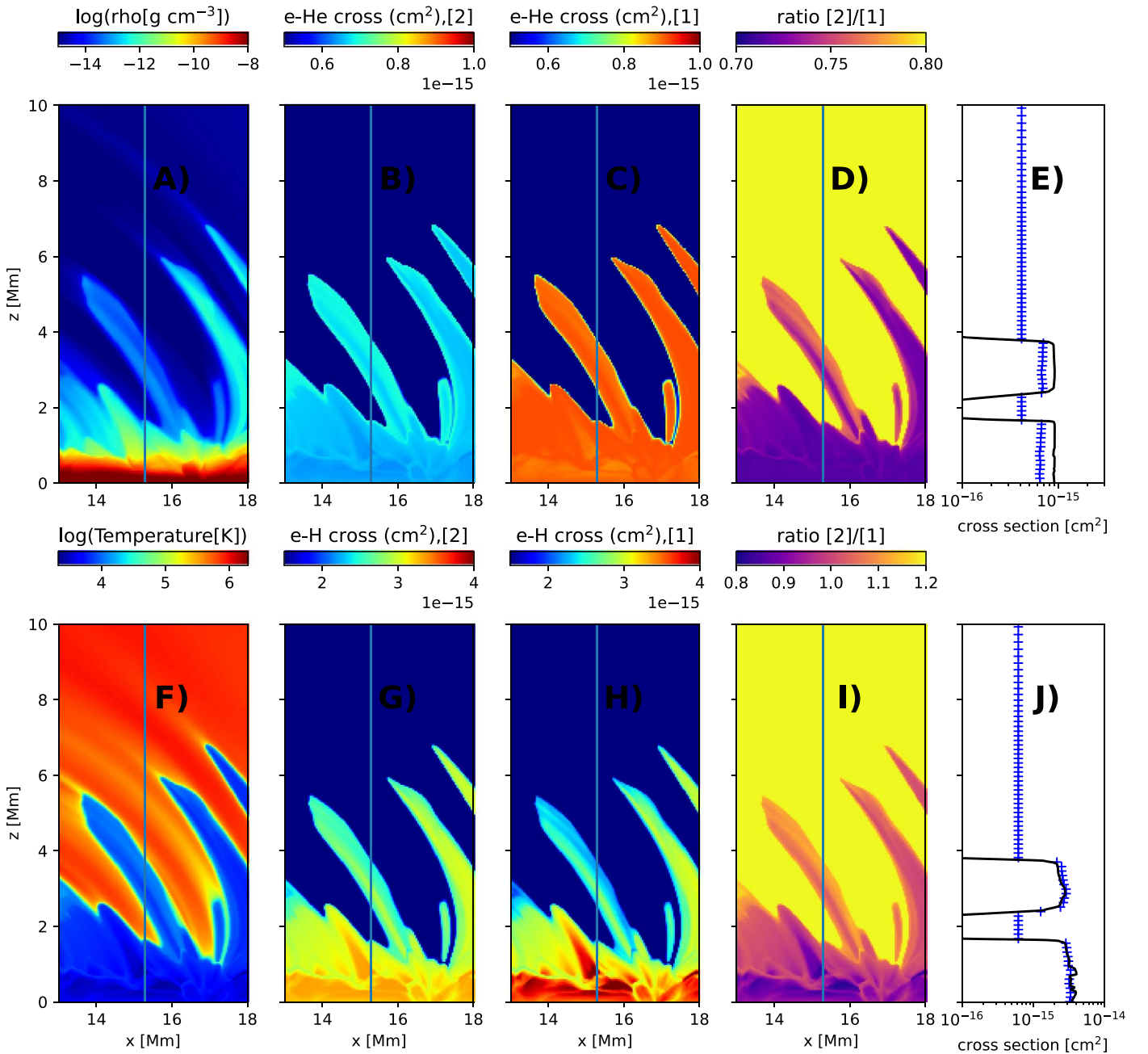


Figure 2. Distribution of the collisional cross section in a 2.5D simulation of *Bifrost* (see Section 4.2, and Martínez-Sykora et al. 2019; Martínez-Sykora et al. 2018) representing the solar atmosphere. Top and bottom: e–H and e–He interactions. From left to right: distribution of the logarithm of the total mass density (top) in g cm^{-3} and temperature (bottom) in kelvin, distribution of the cross section $C_{e,H}$ and $C_{e,He}$ from [A2] in cm^2 , distribution of $4/3 \Omega_{e,H}^{1,1}$ and $4/3 \Omega_{e,He}^{1,1}$ in cm^2 [A1], ratio $C_{e,\alpha}/(4/3 \Omega_{e,\alpha}^{1,1})$, $\alpha \in \{H, He\}$ and a 1D distribution of the cross sections C and $4/3 \Omega^{1,1}$ at $x = 15.2 \text{ Mm}$. The full black line and the blue line with crosses correspond to the cross section calculated with approaches [A1] and [A2], respectively.

the collision frequency between two neutral hydrogen atoms depends only on the number density of neutral hydrogen and temperature, similar results as those shown presented in Figure 3 can also be seen in Figure 6. From regions [A] to [B], in [A2] (panel (B)), the collision frequency decreases more slowly than in [A1] (panel (C)). In region [C], the collision frequency is lower in [A1] than in [A2]. For the same reason as explained in the previous section, the ratio presented in Figure 6(D) is identical to the ratio presented in Figure 5(C), i.e., it ranges from 10 to 20.

4.5. Ion–Neutral Interactions

4.5.1. Interactions Involving Resonant Charge Transfer

In Bruno et al. (2010), the collision integrals associated with interactions that consider resonant charge transfer are composed of two terms associated with elastic and charge-exchange contributions. Generally, the collision integrals are approximated by the following formula:

$$\Omega^{(l,s)} = \sqrt{(\Omega_{\text{elastic}}^{(l,s)})^2 + (\Omega_{\text{ch-ex}}^{(l,s)})^2}, \quad (13)$$

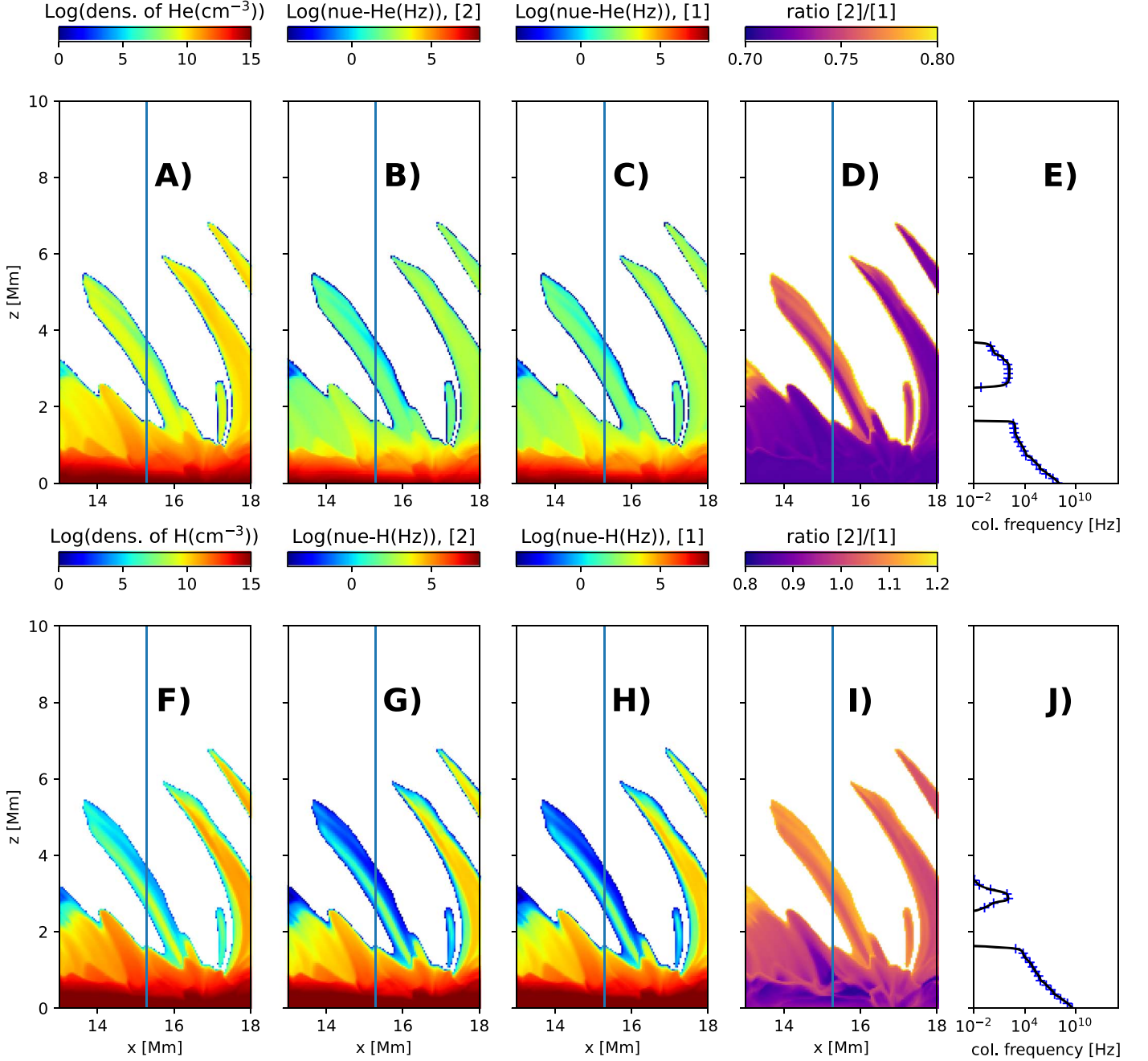


Figure 3. Distribution of the collision frequencies in the 2.5D numerical simulation for the ϵ -H and ϵ -He interactions. Top and bottom: ϵ -He and ϵ -H interactions. From left to right: distribution of the logarithm of the helium number density (top) and hydrogen number density (bottom) in cm^{-3} , distribution of the logarithm of the collision frequency $\nu_{\epsilon,\alpha}^{\text{col},[2]}$, $\alpha \in \{\text{H, He}\}$ in s^{-1} [A2], distribution of the logarithm of $\nu_{\epsilon,\alpha}^{\text{col},[1]}$, $\alpha \in \{\text{H, He}\}$ in s^{-1} in [A1], ratio $\nu_{\epsilon,\alpha}^{\text{col},[2]}/\nu_{\epsilon,\alpha}^{\text{col},[1]}$, $\alpha \in \{\text{H, He}\}$, and a 1D distribution of the collision frequencies at $x = 15.2$ Mm. The full black line corresponds to the collision frequency calculated in [A1]. The blue line with crosses corresponds to the collision frequency calculated in [A2].

where the charge-exchange collision integral $\Omega_{\text{ch-ex}}^{(l,s)}$ has been computed by following the approach of Devoto (1968). This approach has been fitted by Bruno et al. (2010) with a function that depends on the temperature. For approaches [A1] and [A2], we refer to Table 2 for further details about the calculation of $\Omega^{1,1}$ and C . In [A3], a formula of the cross section as function of the thermal speeds of ions and neutrals has been considered.

At the top of Figure 7, we compare the distribution of the cross sections associated with the H-H^+ interaction for the three approaches. At the bottom of Figure 7, we show the

distribution of the cross section associated with the He-He^+ and He-He^{++} interaction. The cross sections associated with the H-H^+ interaction are decreasing with temperature (top panel of Figure 7). For all the considered range of temperatures, the cross sections in [A1] are lower than in [A2]. The oscillations of the cross section at lower temperature in [A2] are associated with quantum effects in Vranjes & Krstic (2013), as presented in Figure 4 for the H-H interaction.

Figure 8 has the same format as Figure 5, but for the H-H^+ interaction. In summary, the cross sections in [A2] (panel (A)) are higher than in [A1] (panel (B)) for all the regions

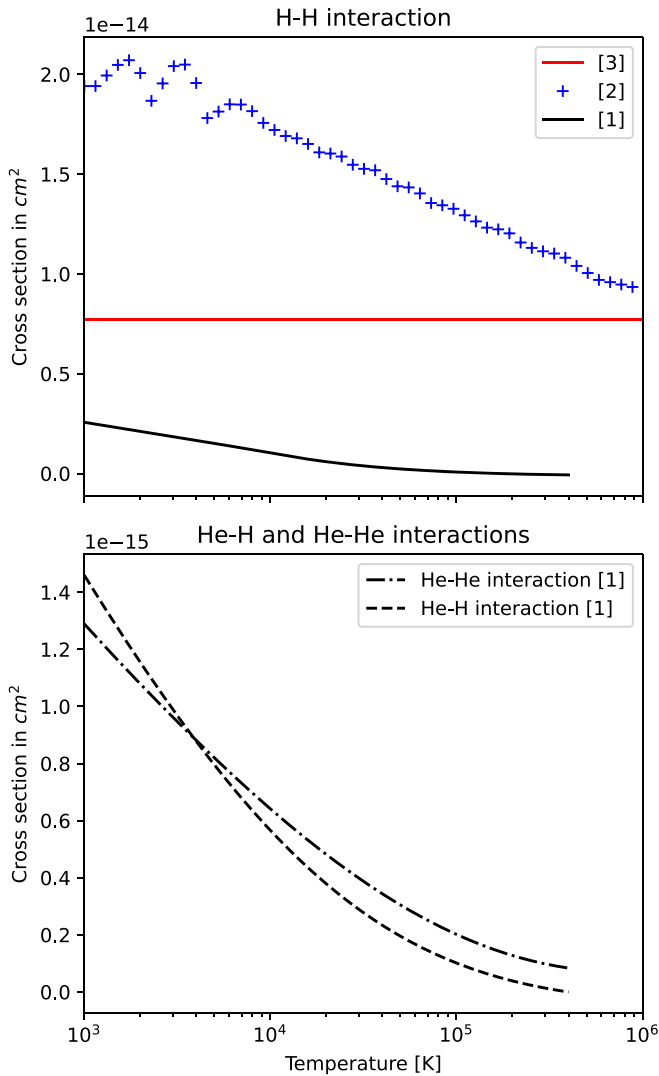


Figure 4. Variation in the cross section (in cm^2) associated with neutral-neutral interactions as a function of the temperature (in kelvin). Top: cross section associated with the H-H interaction based on the three formalisms presented in this section. The full red and black lines correspond to the cross section (in cm^2) of [A3] and [A1], respectively, and the blue line with crosses corresponds to the cross section in [A2]. Bottom: cross sections associated with the He-He and He-H interactions based on [A1].

considered, as expected from the cross-section differences shown in the top panel of Figure 7. The ratio of the two approaches ranges from 1.2 to 1.5 (panel (C)). In region [D], the ratio reaches approximately 1.2. The strong variability of the cross sections in regions [A] and [B] is due to the quantum effects at lower temperatures, as shown in Figure 7. Similarly as in the previous sections, the distribution of the ratio obtained in Figure 8(C) can easily be explained by the top panel of Figure 7. For the considered range of temperature, [A1] is slightly smaller than [A2] and the difference between the two curves is slightly decreasing with temperature. Therefore, the ratio of the two approaches is slightly decreasing from 1.2 to 1.5 from region [A] to region [D], as shown in Figure 8(C).

Figure 9 has the same format as Figure 6, but for the H-H⁺ interaction. Additionally, we also compute the distribution of the number density of H⁺ (Figure 9(A)). At the bottom of region [A], in both approaches (panels (B) and (C)), the collision frequency is small and ranges approximately from

10^{-3} s^{-1} to 10^{-2} s^{-1} . For the upper layers, i.e., from regions [B] to [D], the collision frequencies range from 10^1 to $10^{4.5} \text{ s}^{-1}$. For the same reason as explained in the previous section, the ratio presented in Figure 9(D) is identical to the ratio presented in Figure 8(C). Therefore, the ratio of collision frequencies between the two approaches is ranging from 1.2 to 1.5 in the entire solar atmosphere.

Similarly as previous sections, large differences have been obtained between approaches [A1] and [A2], whereas identical data associated with the transport cross sections have been considered (see Krstic & Schultz 1999, 1998). These disparities can be explained by the inconsistency of [A2] with the formalism of collision integrals.

4.5.2. Interactions Involving Ionized Metals and Neutral Species

In this section, we focus on the interactions involving ionized metals and neutral hydrogen, known as elastic molecular Maxwell interactions, such as the α -Fe⁺, α -Mg⁺, α -O⁺, α -Ne⁺, and α -Ni⁺, $\alpha \in \{\text{H}, \text{He}\}$ interactions. Similarly as in the previous sections, for approaches [A1] and [A2], we refer to Table 2 for further details about the calculation of $\Omega^{1,1}$ and C. Note that the collision frequencies associated with these particular interactions are independent of the temperature, but depend on the number densities of the ionized metals.

Similarly as in the previous sections, we have calculated the distributions of the logarithm of the collision frequencies in s^{-1} for approaches [A1] and [A2] for all the interactions between ionized metals and neutral hydrogen or helium in the same 2.5D simulation. In this section, we show our calculations only for ionized metals and neutral hydrogen interactions in approaches [A1] and [A2], presented in the top and middle row of Figure 10. Indeed, all the other approaches can easily be determined from the ionized metals and neutral hydrogen interactions by a scale factor, thus, it is not necessary to show their distributions here.

In regions [A] and [B], in the bottom row of Figure 10, the density of ionized metals differs by several orders of magnitude. In summary, from the photosphere to the bottom of the chromosphere, the most dominant metal species are Fe⁺ and Mg⁺. As a matter of fact, when the ionization is in statistical equilibrium, in extended areas of regions [A] and [B], the dominant ion is Fe and Mg; compare to the number of protons (Figure 9(A)). In these regions, the collision frequencies associated with both the H-Fe⁺ and H-Mg⁺ interactions in [A1] are more than one order of magnitude lower than in [A2]. Note that these regions of the solar atmosphere are poorly populated by Ne⁺, O⁺, and Ni⁺.

In region [C], in the spicule, the most dominant ionized metal species are Ne⁺ and O⁺. However, there is still a non-negligible population in Fe⁺ and Mg⁺. Therefore, in this region, the most dominant collision frequencies are those associated with the interactions H-Ne⁺ and H-O⁺. However, these collision frequencies are much lower than those associated with Fe⁺ and Mg⁺ in region [A] and region [B] by 2 to 4 orders of magnitude. In region [D], all the collision frequencies associated with these interactions can be considered negligible. Note that for all the interactions considered for all the regions considered, the ratio obtained between [A2] and [A1] ranges from 200 to 600, as shown in Figure 11.

Additionally, in [A1], the collision frequencies associated with neutral helium and ionized metals are found to be identical to those associated with neutral hydrogen and ionized metals

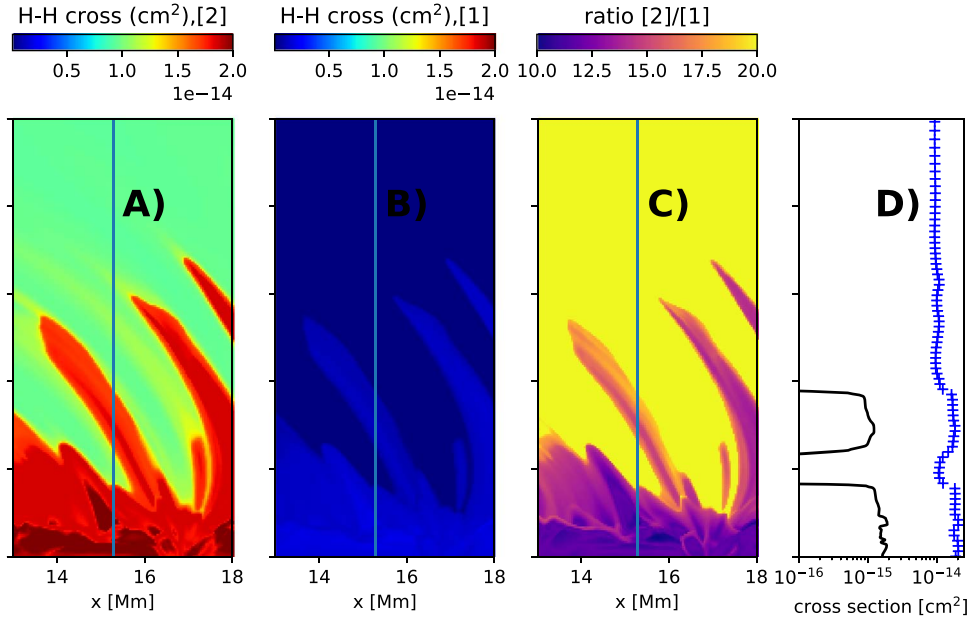


Figure 5. Distribution of the collision cross section in the 2.5D numerical simulation representing the solar atmosphere (Section 4.2). From left to right: distribution of the cross section $C_{H,H}$ from [A2] in cm^2 , distribution of $4/3 \Omega_{H,H}^{1,1}$ in cm^2 from [A1], the ratio $C_{H,H}/(4/3 \Omega_{H,H}^{1,1})$, and a 1D distribution of the cross sections $C_{H,H}$ and $4/3 \Omega_{H,H}^{1,1}$ at $x = 15.2 \text{ Mm}$. The full black line corresponds to the cross section based on the formalism introduced in [A1]. The blue line with crosses corresponds to the cross section introduced in [A2].

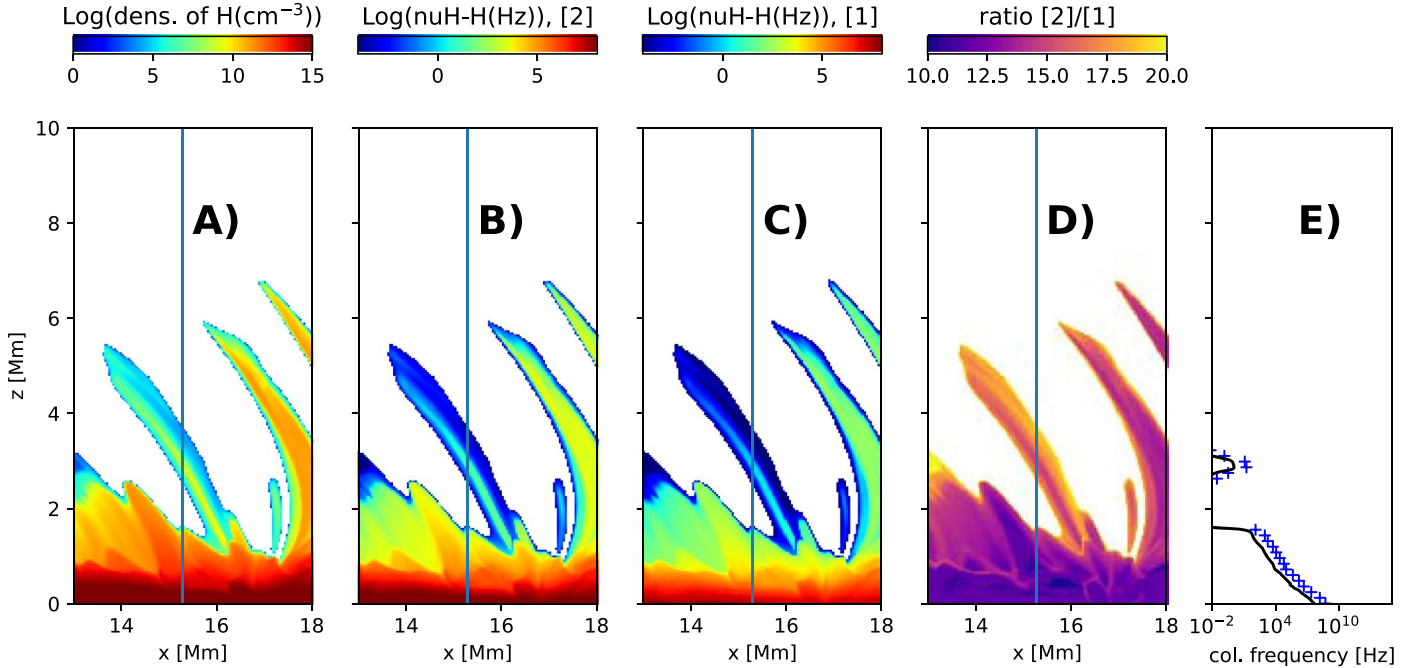


Figure 6. Distribution of the collision frequencies in the 2.5D simulation representing the solar atmosphere for the H–H interaction (Section 4.2). From left to right: distribution of the logarithm of the density of neutral hydrogen H in cm^{-3} , distribution of the logarithm of the collision frequency $\nu_{H,H}^{\text{col},[2]}$ in s^{-1} from [A2], distribution of the logarithm of $\nu_{H,H}^{\text{col},[1]}$ in s^{-1} from [A1], the ratio $\nu_{H,H}^{\text{col},[2]}/\nu_{H,H}^{\text{col},[1]}$, and a 1D distribution of the collision frequencies at $x = 15.2 \text{ Mm}$. The full black line corresponds to the collision frequency based on the formalism introduced in [A1]. The blue line with crosses corresponds to the collision frequency used in [A2].

by a factor of $\sqrt{\alpha_{\text{pol}}^{\text{He}}/\alpha_{\text{pol}}^{\text{H}}}$, which depends on the polarizability coefficients of helium and hydrogen (see Section B for further details).

In summary, our calculations have shown that the collision frequencies associated with ionized metals and neutral hydrogen interactions are not negligible from regions [A] to [B] in approaches [A1] and [A2]. Note that [A1] and [A2] differ enormously from region [A] to [B]. The large disparities

obtained between the two approaches are due to the different definitions of the cross section. Indeed, in [A2], a simplified definition of the cross section from Vranjes et al. (2008) is used, where a formula based on a ratio of mass between neutrals and metals has been considered, as presented in Table 2. However, in [A1], the collision integral has been calculated from the integration of an interaction potential that follows a polarization model. Outside of these regions, our

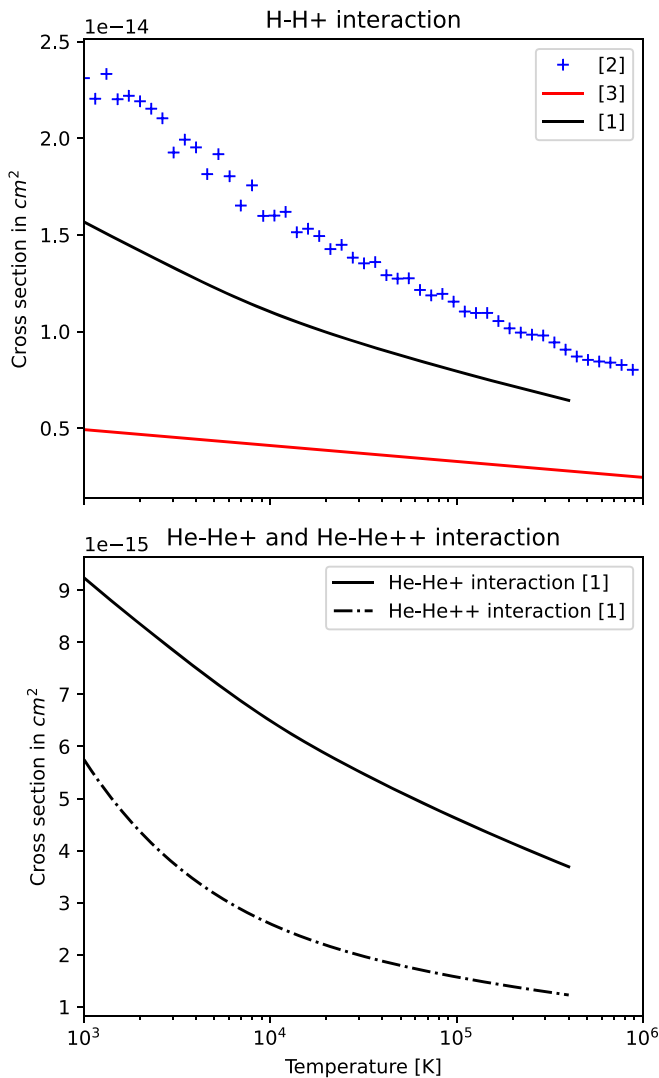


Figure 7. Same layout as Figure 4 for H–H⁺ (top), and He–He⁺, and He–He⁺⁺ (bottom).

results have shown that these interactions have negligible effects compared with ion–neutral interactions with resonant charge transfer, neutral–neutral, and electron–neutral interactions.

4.5.3. Interactions without Resonant Charge Transfer

In this subsection, we focus on the H–He⁺, He–H⁺, and H–He⁺⁺ interactions. In [A3], a constant cross section $C = 1.16 \times 10^{-14} \text{ cm}^2$ has been used for all ion–neutral interactions that do not involve resonant charge transfer. In [A2], only data for the He–H⁺ are provided. Note that the same references for the momentum transport cross sections have been considered in approaches [A1] and [A2].

At the top of Figure 12, similarly as for the ion–neutral and neutral–neutral interactions, the cross sections that follow [A2] are higher than in [A1] by slightly less than one order of magnitude. For temperatures higher than 10^4 K, the cross section appears to be negligible in [A1] but is constant in [A2] and equal to approximately $2.5 \times 10^{-15} \text{ cm}^2$. The oscillations obtained at lower temperatures are associated with quantum effects, similarly as in Figure 7. At the bottom of Figure 12, the cross section associated with the H–He⁺ interaction is smaller

than for H–He⁺⁺. For temperatures higher than 2×10^4 K, the cross section associated with H–He⁺ interaction is considered negligible.

Figure 13 has the same format as Figure 8, but for the He–H⁺ interaction. In summary, from region [A] to region [C], in Figure 13(C), the ratio of the two approaches ranges from 7.5 to 12.5. In region [D], the two approaches differ largely as in [A1] the cross section is assumed to be negligible, whereas in [A2] it is constant. Similarly as in the previous sections, the distribution of the ratio of [A1] and [A2] obtained in panel (C) from Figure 13 is due to the differences obtained on the cross-section dependence on temperature, as presented in Figure 12.

Similarly as in the previous sections, Figure 14 has the same format as Figure 8 for the He–H⁺ interaction. The 2D distributions of the collision frequencies are similar to those presented for the H–H, e–H, and e–He interactions in Figures 6 and 3. In particular, in [A2], the distribution of the cross sections for the H⁺–He interaction is almost identical to the distribution associated with the e–He interaction presented in Figure 3 because both of these distributions depend on the number density of neutral helium. In region [D], the collision frequency is negligible because helium is mostly ionized. Finally, the two approaches differ by approximately one order of magnitude (ratio between 7.5 and 12.5).

5. Quasi-neutral Fluid Limit and Ambipolar Diffusion

As shown in the previous sections, large differences have been obtained between approaches [A1] and [A2] or [A3] for most of the interactions considered in \mathfrak{M} . These differences are likely to have an impact on the macroscopic effects of various mechanisms in the solar atmosphere. This can be illustrated with the ambipolar diffusion, for example.

5.1. Brief Description of Ambipolar Diffusion

Most studies of the solar atmosphere describe the interaction between the magnetic field and plasma using a single-fluid MHD approximation. This is sometimes sufficient, but single-fluid MHD timescales may become comparable to collision frequencies in the solar atmosphere. The upper chromosphere, transition region, and corona are nearly collisionless. Consequently, slippage between, for instance, ions and neutral particles, or interactions between separate species (see Bai & Stone 2011; Leake et al. 2014; Martínez-Sykora et al. 2015; Ballester et al. 2018; Martínez-Sykora et al. 2019) may play important roles in the dynamics and energetics of the atmosphere. Several studies have tried to approximate ion–neutral interaction effects in single-fluid MHD models by using the generalized Ohm law, which includes the ambipolar diffusion (see Cowling 1962; Braginskii 1965; Leake & Arber 2006; Khomenko & Collados 2012, Ballester et al. 2018).

Single-fluid MHD numerical models that include ambipolar diffusion assume either single species (hydrogen) or several species (hydrogen, helium, or metals). This approach is generally used to simulate the solar atmosphere and accounts for ion and neutral interactions while retaining in a single-fluid approach description. In this approach, first the quasi-neutrality assumption is considered, and then all ionized species move at the same speed, and similarly for the neutrals. The resulting

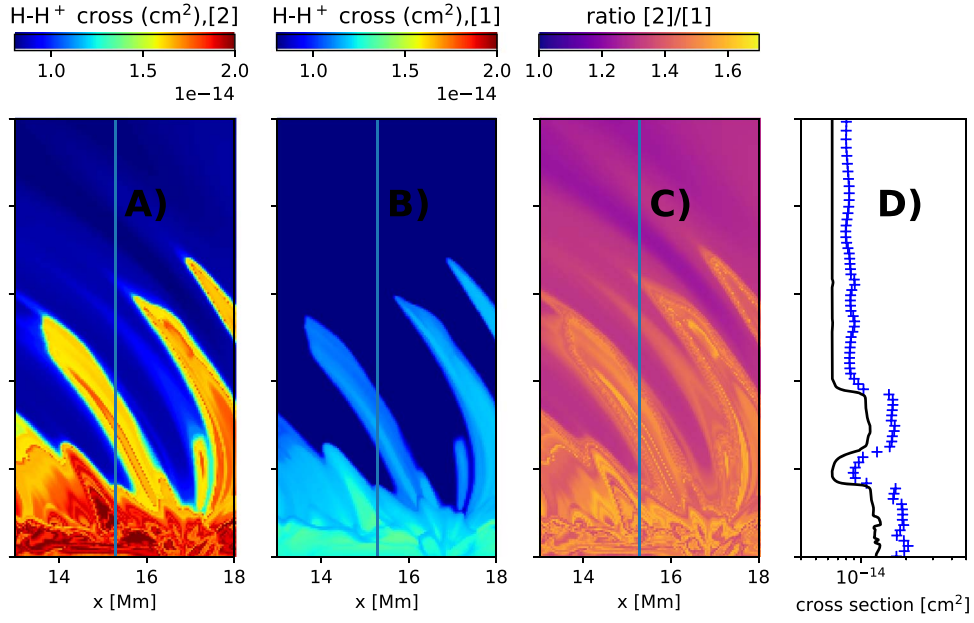


Figure 8. Same layout as Figure 5 for H-H⁺ interactions.

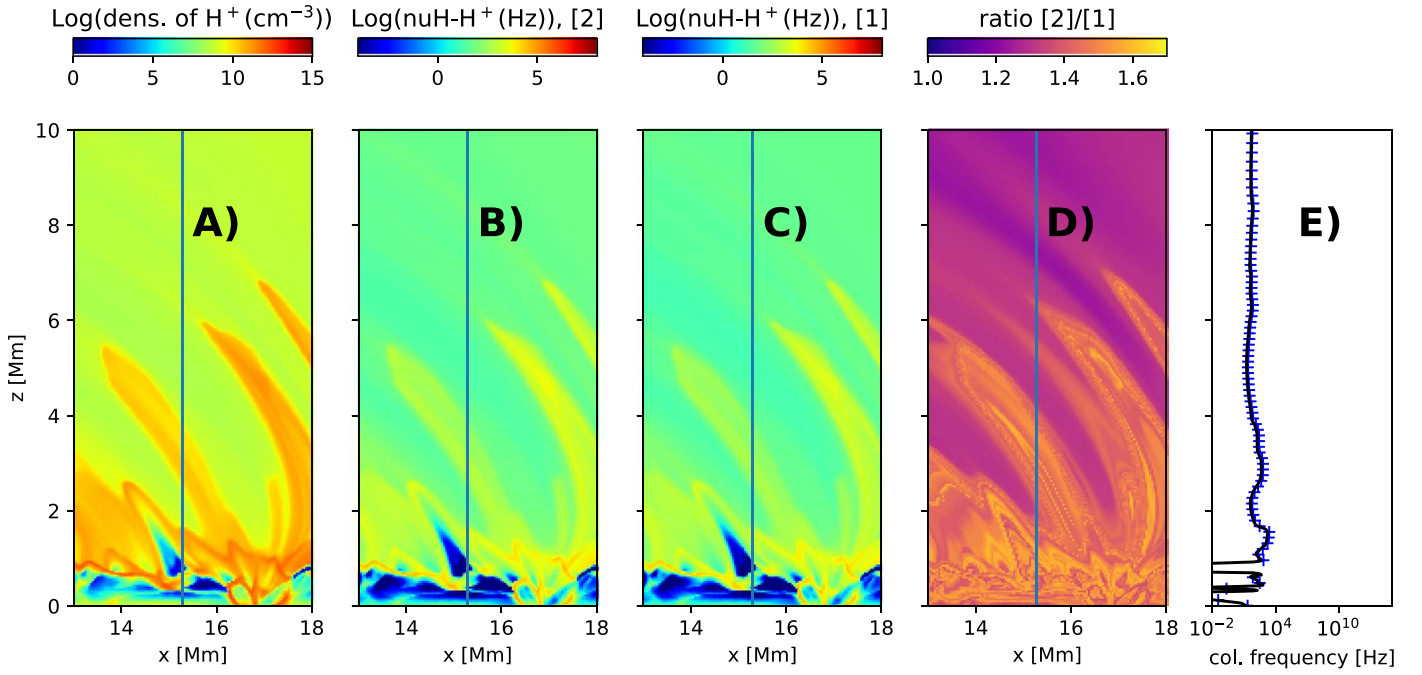


Figure 9. Same layout as Figure 6 for H-H⁺ interactions. Panel (A) shows the number density of H⁺.

magnetic induction equation is as follows:

$$\frac{\partial \mathbf{B}}{\partial t} = \nabla \wedge \left(\mathbf{u}_0 \wedge \mathbf{B} + \eta_{\text{amb}} \mathbf{J} \wedge \mathbf{B} \wedge \mathbf{B} + \frac{\mathbf{J} \wedge \mathbf{B}}{n_e q_e} \right), \quad (14)$$

where \mathbf{B} is the magnetic field, \mathbf{u}_0 is the hydrodynamic velocity, \mathbf{J} is the total density current, n_e is the number density of the electrons, q_e is the charge of the electrons, and η_{amb} is the ambipolar diffusion coefficient. The second term in the right-hand side is the ambipolar diffusion, and the last term is the Hall term. The ambipolar diffusion coefficient depends on the

ion-neutral collision frequency and ionization fraction as follows:

$$\eta_{\text{amb}} = \frac{(\rho_n / \rho)^2 |\mathbf{B}|^2}{\rho_n \nu_{ni}}; \quad (15)$$

where ρ is the total mass density, and ρ_n is the total neutral mass density, and ν_{ni} is the neutral-ion collision frequency. This expression was derived from a single species, e.g., hydrogen. In an environment with several species, typically, one assumes that all ions and all neutrals move together (e.g.,

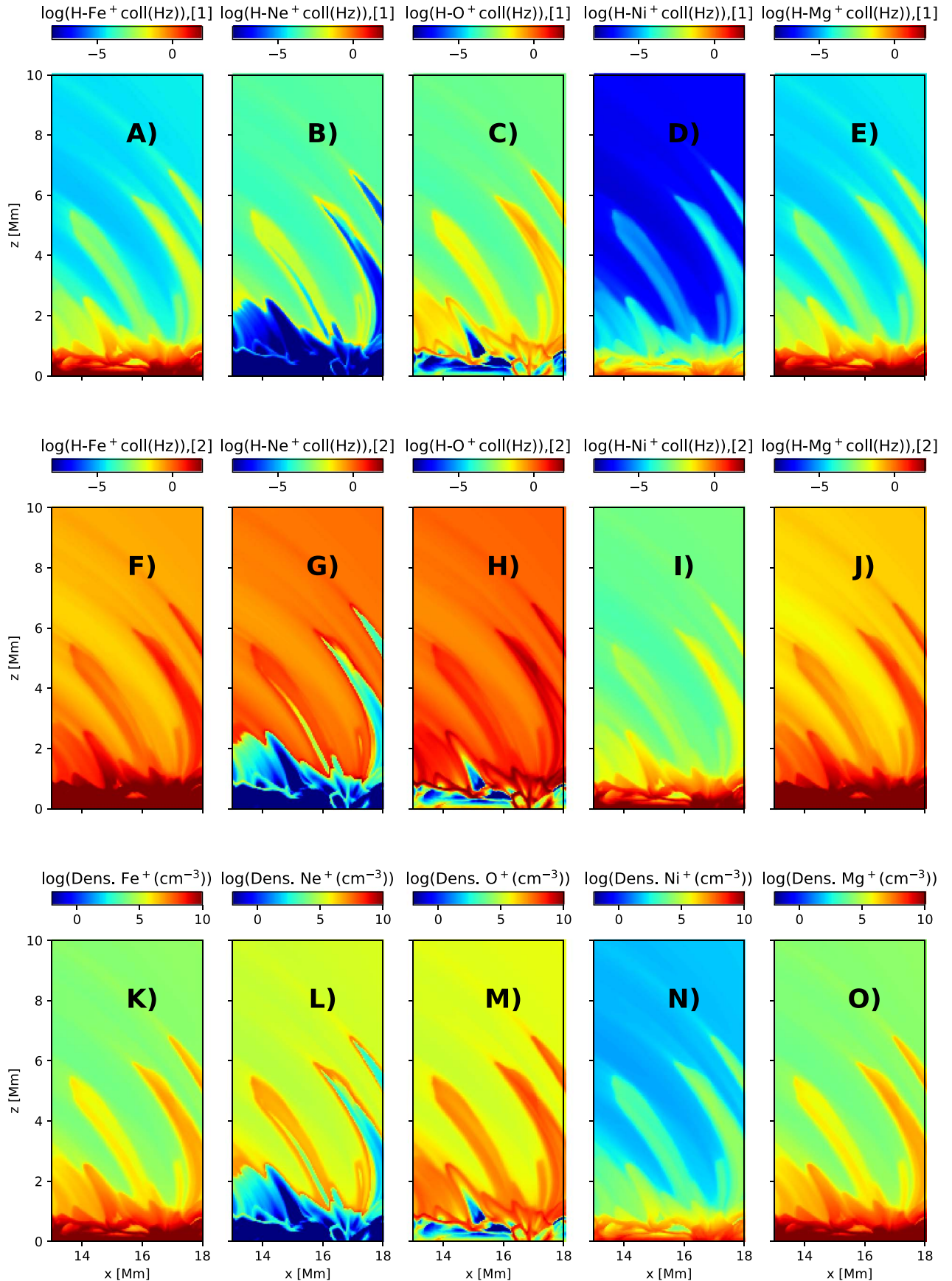


Figure 10. In the top and middle row: distribution of the collision frequencies associated with ionized metals and neutral hydrogen interactions for approaches [A1] and [A2], such as H-Fe⁺, H-Ne⁺, H-O⁺, H-Ni⁺, and H-Mg⁺, in the 2.5D simulation representing the solar atmosphere (Section 4.2). From left to right: distribution of the logarithm of the collision frequency ν^{col} in s^{-1} associated with the H-Fe⁺, H-Ne⁺, H-O⁺, H-Ni⁺, and H-Mg⁺ interactions. In the bottom row, from left to right: distribution of the logarithm of the density in cm^{-3} of Fe⁺, Ne⁺, O⁺, Ni⁺, and Mg⁺.

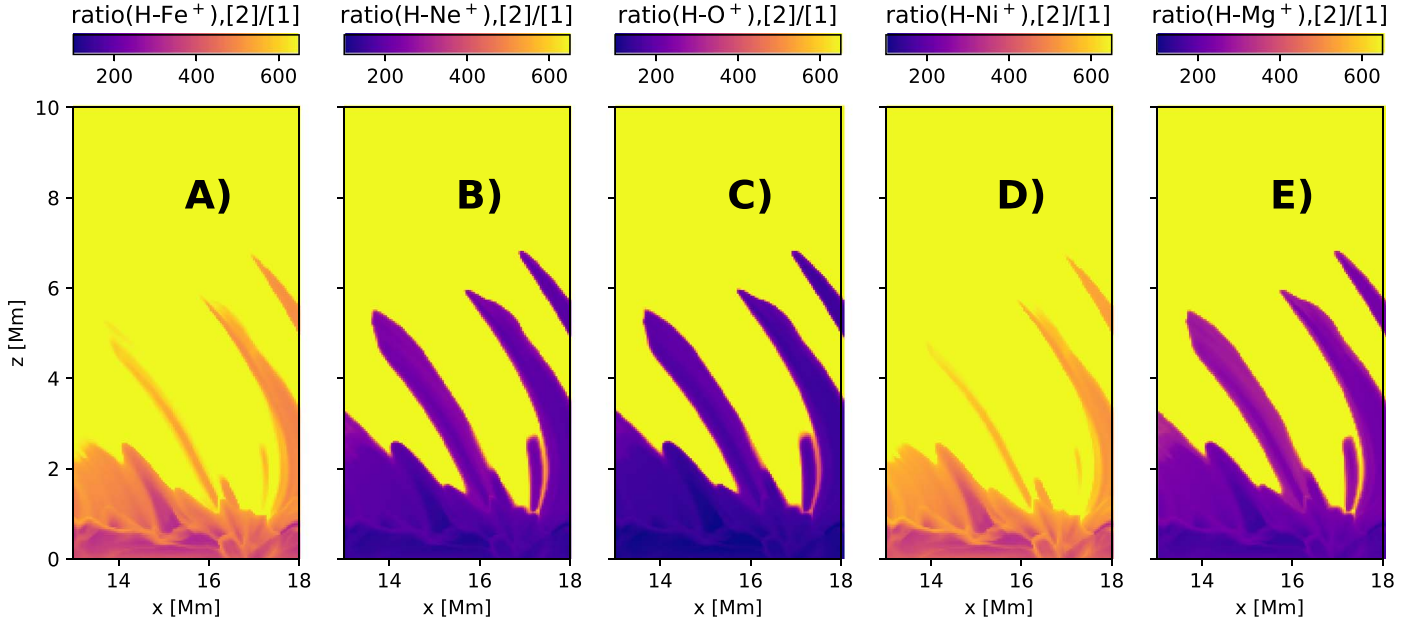


Figure 11. Distribution of the ratio of the collision frequencies between [A2] and [A1] associated with H and ionized metals interactions in the 2.5D radiative MHD simulation (Section 4.2). From left to right: ratio $\nu^{\text{col},[A2]}/\nu^{\text{col},[A1]}$, associated with H-Fe⁺, H-Ne⁺, H-O⁺, H-Ni⁺, and H-Mg⁺ interactions.

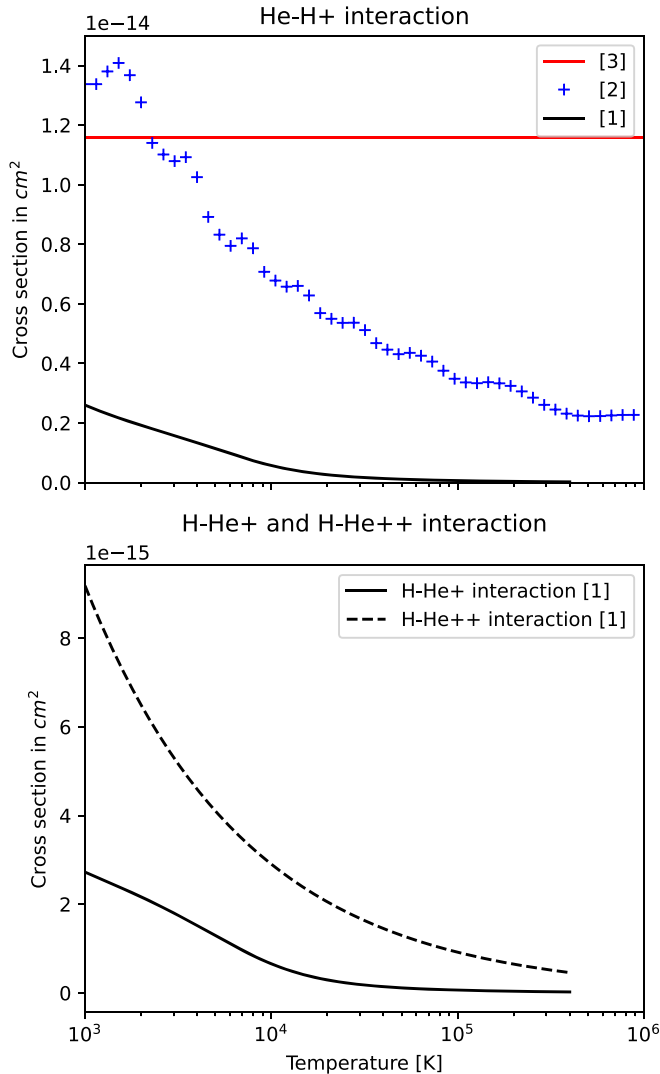


Figure 12. Same layout as Figure 4 for He-H⁺ (top), and H-He⁺, H-He⁺⁺, and He-He⁺⁺ (bottom).

Martínez-Sykora et al. 2012). In this case, the ion–neutral collision frequency is defined as

$$\nu_{ni} = \sum_{a0, a'j} \rho_{a0} \frac{m_{a'j}}{m_{a'j} + m_{a0}} \nu_{a0a'j}^{\text{col}}, \quad \mathcal{J} \geq 1. \quad (16)$$

To compute the ambipolar diffusion shown in the left panel of Figure 15, the collision frequency ν_{ni} has been calculated following Equation (16), where each $\nu_{a0a'j}^{\text{col}}, \mathcal{J} \geq 1$ is defined from [A1]. For convenience, we rename the ambipolar diffusion coefficient $\eta_{\text{amb}}^{[1]}$. Additionally, in the middle panel of Figure 15, we have also compared with another definition of the ambipolar diffusion, called $\eta_{\text{amb}}^{[2]}$, where each collision frequency involved in Equation (16) is replaced by the collision frequency calculated with [A2] as $\nu^{\text{col},[A2]}$.

The ambipolar diffusion term increases with temperature within $T \in [10^3, 10^5]$ K and decreases with the total density within $\rho \in [10^{-13}, 10^{-5}]$ kg m⁻³. The ratio shows strong differences in the right panel of Figure 15, where the ratio is ranging from 10^{-3} to 10^{-1} . The high ratio at lower temperature, which corresponds to the bottom horizontal purple stripe, i.e., below $T = 4000$ and $T = 7000$ K, is due to the difference in the approach used for the interactions between ionized metals and neutral species between approaches [A1] and [A2] as the collision frequencies associated with these interactions are dominating at these thermodynamic conditions (see Section 4.5.2 for further details). The strong differences obtained in Figure 15 are expected as the various collision frequencies have shown large differences in these conditions, according to the results presented in the previous sections. However, it is difficult to determine which of the many collision frequencies dominates the differences obtained between approaches [A1] and [A2].

In summary, in these conditions, which encompass photospheric and chromospheric conditions, the ambipolar diffusion $\eta_{\text{amb}}^{[1]}$ is much higher than $\eta_{\text{amb}}^{[2]}$ by 1 to 2.5 orders of magnitude. In this context, the decoupling between neutrals and ionized species is weaker for [A1] than for [A2]. In terms of energetics, the approach involved in [A1] most likely will lead to a higher

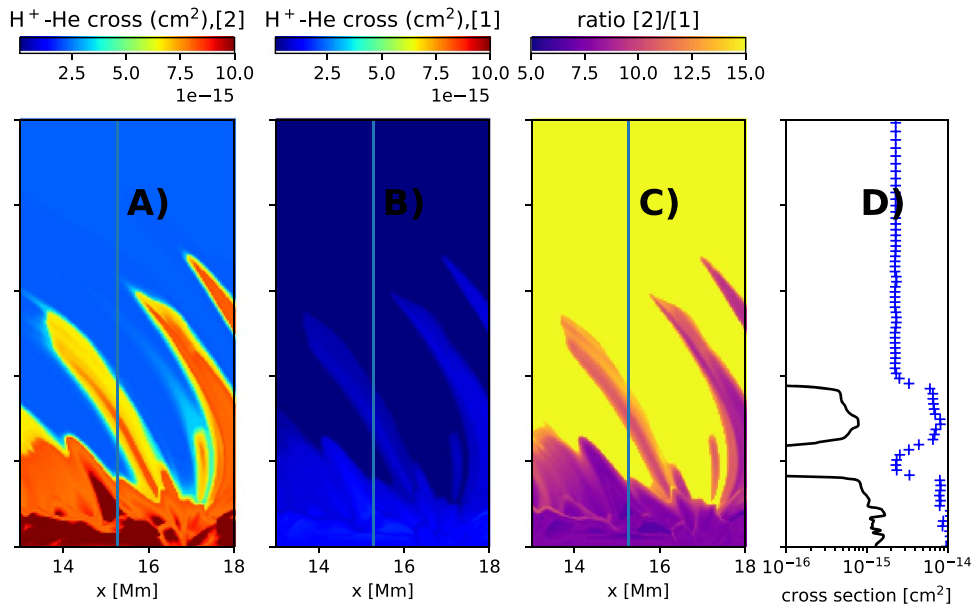


Figure 13. Same layout as Figure 5 for He-H⁺ interactions.

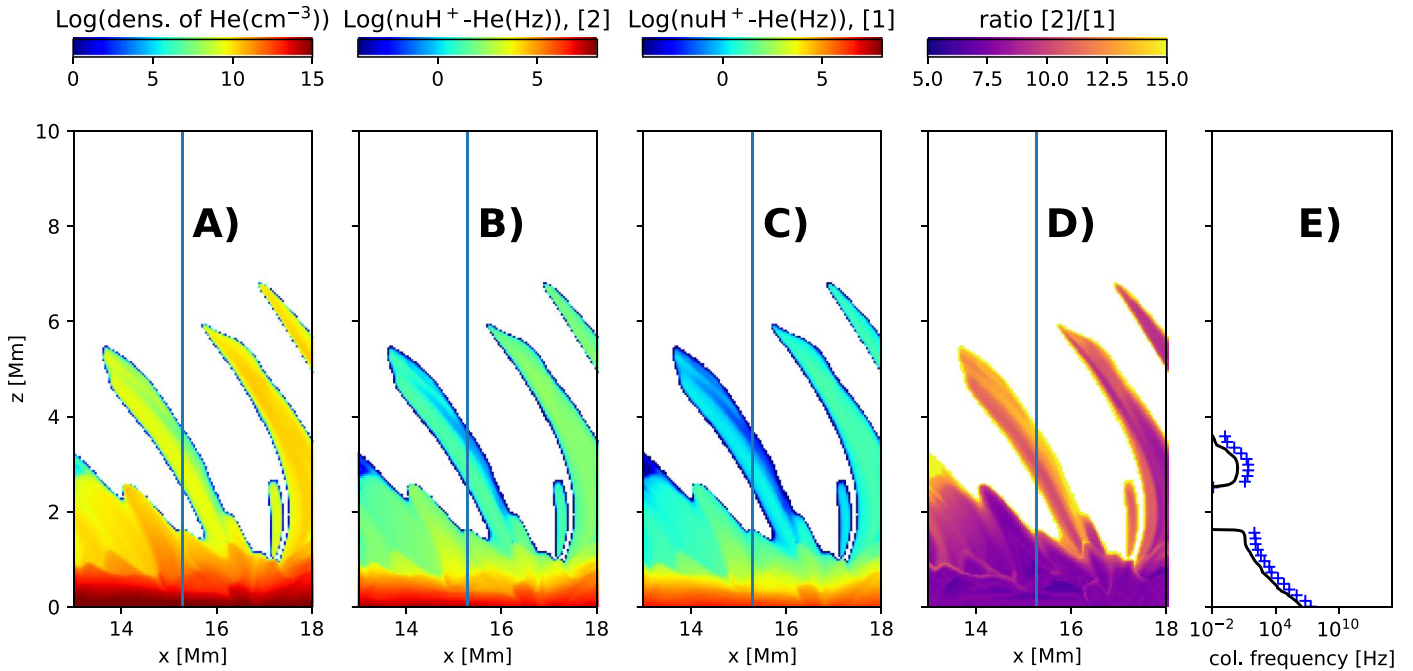


Figure 14. Same layout as Figure 6 for He-H⁺ interactions. Panel (A) shows the number density of He.

energy release in these regions of the solar atmosphere due to the larger decoupling between ions and neutrals. In particular, in upper chromospheric conditions or spicules, our calculations have shown that the ambipolar diffusion for [A1] is higher than for [A2] by slightly more than one order of magnitude. These results suggest that previous calculations of the macroscopic impact of ambipolar diffusion should be revisited and are likely larger than previous work suggests.

5.2. Results Based on Different Mixtures

In order to identify the impact of the different species involved in \mathfrak{M} on the ambipolar diffusion coefficient, three

mixtures have been considered to recalculate the ambipolar diffusion coefficient. These mixtures are

1. a hydrogen mixture composed of $\mathfrak{M}_H = \{H^+, H, e\}$
2. a helium-hydrogen mixture composed of $\mathfrak{M}_{He-H} = \mathfrak{M}_H \cup \{He, He^+, He^{++}\}$
3. the mixture involving all species, including ionized metals, $\mathfrak{M} = \mathfrak{M}_{He-H} \cup \{Ne^+, Fe^+, Mg^+, Ni^+, O^+\}$.

In the first column of Figures 16(A), (E), and (I) which represents our calculations based on the mixture with hydrogen \mathfrak{M}_H , in regions [A] and [B], the distribution of the ambipolar diffusion covers a wide range of values from $10^7 \text{ cm}^2 \text{ s}^{-1}$ to more than $10^{17} \text{ cm}^2 \text{ s}^{-1}$. This is because of the distribution of

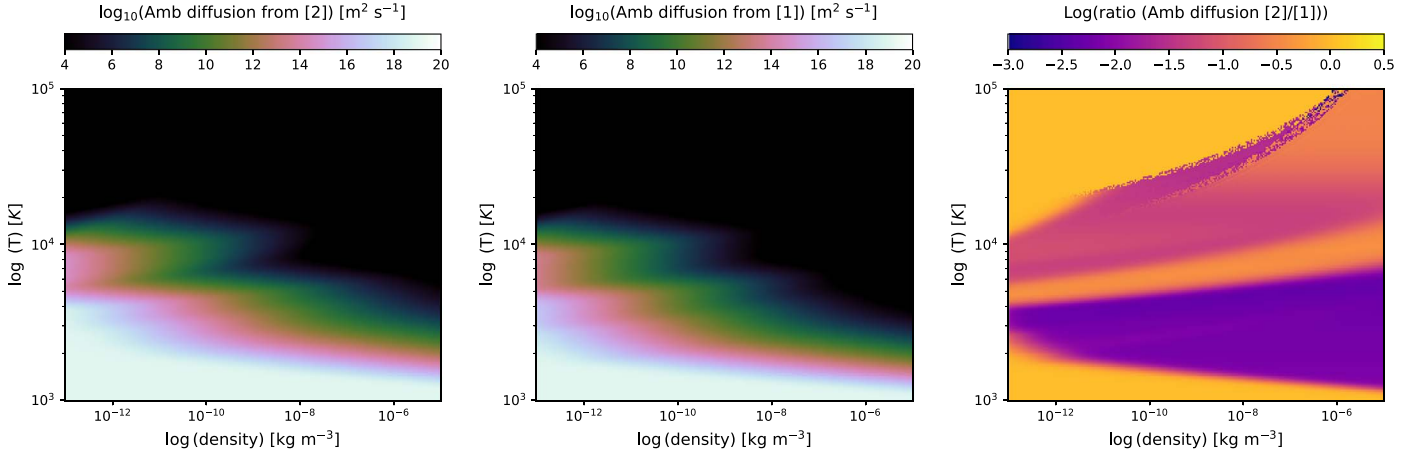


Figure 15. Left and middle: distribution of the logarithm of the ambipolar diffusion term $\eta_{amb}^{[2]}$ and $\eta_{amb}^{[1]}$ in $m^2 s^{-1}$ as a function of the logarithm of the total density ρ in $kg m^{-3}$ and temperature in kelvin. Right: distribution of the logarithm of the ratio $\eta_{amb}^{[2]}/\eta_{amb}^{[1]}$ as a function of the logarithm of the total density ρ in $kg m^{-3}$ and temperature in kelvin.

the collision frequency between ionized and neutral hydrogen presented in Figure 9. Indeed, the ambipolar diffusion is inversely proportional to the sum of all the possible combinations of collisional frequencies between ionized and neutral species. In the case of \mathfrak{M}_H , only H^+ and H are involved in this definition. In region [C], in [A1], the ambipolar diffusion is decreasing from $10^{11} cm^2 s^{-1}$ to approximately $10^7 cm^2 s^{-1}$. In [A2], which corresponds to panel (E), the distribution of the ambipolar diffusion is similar to [A1] in all the regions of the solar atmosphere, with a ratio ranging between 0.5 and 0.3, as shown in Figure 16(I). In this framework, the ambipolar diffusion in [A2] is lower than in [A1]. This is confirmed in our 1D distribution plot at $x = 15.2 Mm$ with the black line with crosses presented in Figure 16(L). Note that in all approaches, in region [D], the ambipolar diffusion is assumed to be negligible because the plasma is mostly fully ionized.

The situation is quite different for a mixture with helium, as shown in Figures 16(B), (F), and (J)). Indeed, in approaches [A1] and [A2], our calculations show that adding helium species to the mixture causes more spatial variations of the ambipolar diffusion mainly in the upper layers of the solar atmosphere, corresponding to the upper layer of regions [B] and [C]. In particular, the ambipolar diffusion is increasing by several orders of magnitude compared to the hydrogen mixture \mathfrak{M}_H . This change can be attributed to the increase in the density of neutral species due to the presence of neutral helium in region [C], which is not considered in the case based on \mathfrak{M}_H . Indeed, as we saw in Figures 3(A) and (F), there is much more neutral helium than hydrogen in region [C]. In this context, as the ambipolar diffusion is proportional to the total density of neutrals, it is increasing in region [C] in the case based on \mathfrak{M}_{He-H} compared to \mathfrak{M}_H . These results are consistent with those obtained by Nóbrega-Siverio et al. (2020). In Figure 16(J), our calculations show that in region [C], the ambipolar diffusion is significantly lower for [A2] than [A1] (i.e., the ratio is decreasing down to $10^{-1.5}$). Note that this may help to heat the spicules to greater temperatures (De Pontieu et al. 2017a; Chintzoglou et al. 2021), but this will need to be verified with new numerical simulations. These differences in the distribution of the ambipolar diffusion in region [C] are attributed to the collision frequency between neutral helium and protons presented in Figure 14 considered in the approach with \mathfrak{M}_{He-H} . Indeed, in region [C] from Figure 14, one can

notice that the calculated collision frequency is much lower in [A1] than in [A2], thus, the ambipolar diffusion in [A1] is higher by approximately one order of magnitude than in [A2].

In regions [A] and [B], the ratio ranges between $10^{-0.3} \approx 0.5$ and $10^{-0.5} \approx 0.32$ (panel (J)) as in the case based on \mathfrak{M}_H (panel (I)). In addition, in these regions, no differences in the spatial distribution of the ambipolar diffusion between \mathfrak{M}_H and \mathfrak{M}_{He-H} mixtures have been obtained (panels (A)–(B) and panels (E)–(F)). This is mostly due to the fact that these regions are mostly populated by hydrogen species in both approaches.

Finally, if we focus on [A1] and [A2] in the third column of Figure 16 (corresponding to panels (C), (G), and (K)), ionized metals are mostly changing the distribution of the ambipolar diffusion in the bottom layer of the solar atmosphere, corresponding to region [A] and region [B]. Indeed, when ionized metals are considered in the mixture, the ambipolar diffusion drops by several orders of magnitude compared to \mathfrak{M}_{He-H} and \mathfrak{M}_H . In [A1], corresponding to Figure 16(C), it ranges from 10^6 to $10^8 cm^2 s^{-1}$, which is approximately 2 orders of magnitude higher than in [A2]. This variation obtained in both approaches can be explained by the large population of Mg^+ and Fe^+ in region [A], as shown in Figures 10(K) and (O). The collision frequencies associated with $H-Fe^+$ and $H-Mg^+$ interactions are much higher than all the collision frequencies associated with the other ion–neutral interactions (in particular, $H-H^+$) in the bottom of region [A]. Consequently, the ion–neutral collision frequency presented in Equation (16) is much higher in these regions, leading to a large decrease of the ambipolar diffusion coefficient (panel (C)) compared to \mathfrak{M}_H (panel (A)) and \mathfrak{M}_{He-H} (panel (B)). Similar results have been obtained in [A2], as shown in panels (E), (F), and (G).

In summary, these calculations allow us to clearly identify the impact of the different species on the spatial distribution and variation of the ambipolar diffusion coefficient in the solar atmosphere. Our results for single-fluid MHD approaches that include ambipolar diffusion show that calculations based on [A1] could lead to a higher energy release than [A2] in the upper layers of the solar chromosphere and low transition region. It would be still necessary to run a simulation on a solar timescale in order to clearly characterize the difference in the energy release by the two different approaches [A1] and [A2]. However, the results presented here are the first step toward

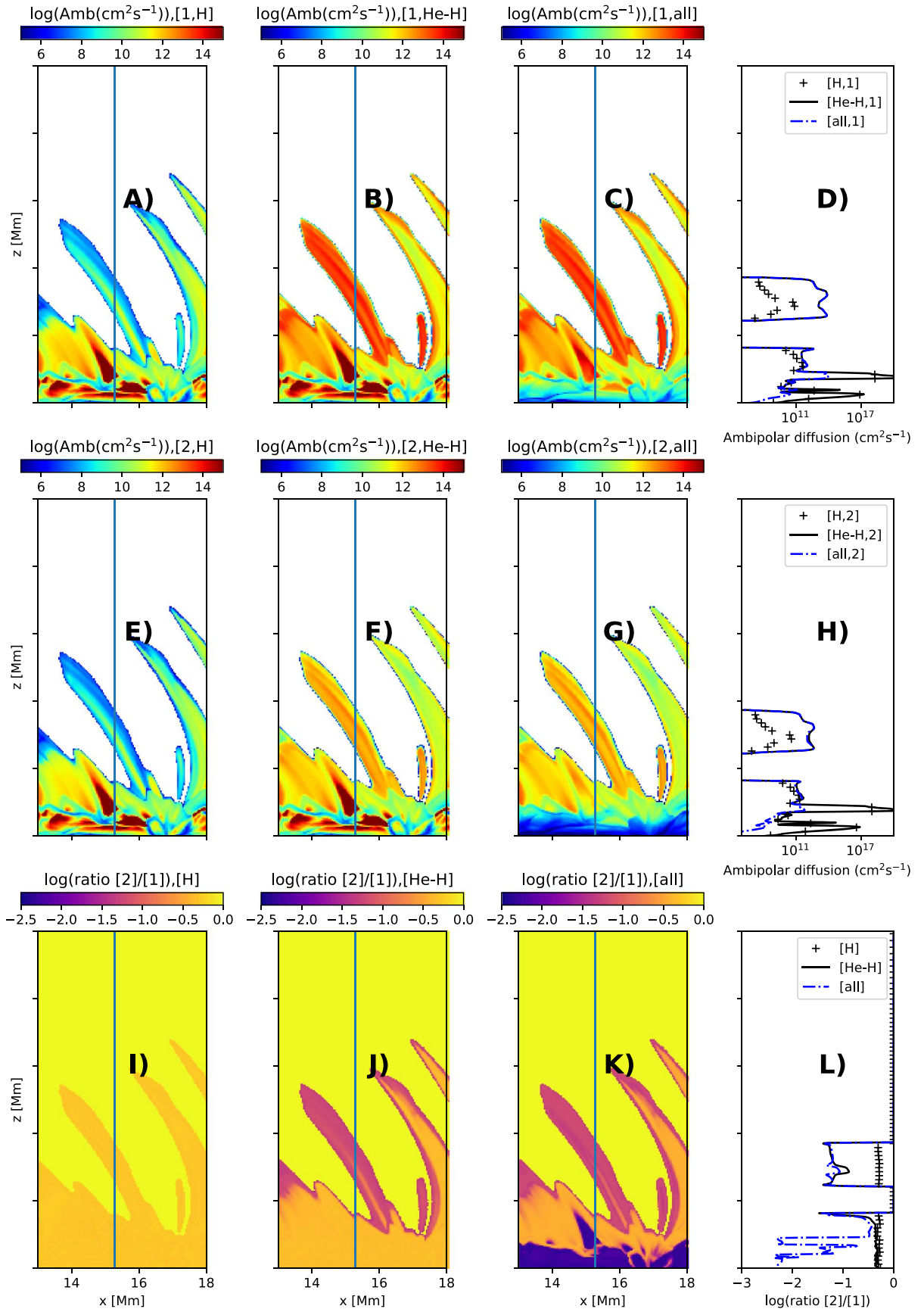


Figure 16. Distribution of the ambipolar diffusion in the 2.5D simulation (Section Section 4.2). From top to bottom: distribution of the logarithm of the ambipolar diffusion $\eta_{\text{amb}}^{[1]}$ and $\eta_{\text{amb}}^{[2]}$ in $\text{cm}^2 \text{s}^{-1}$, and the ratio $\eta_{\text{amb}}^{[2]}/\eta_{\text{amb}}^{[1]}$. From left to right: distribution of the logarithm of the ambipolar diffusion with hydrogen mixture \mathfrak{M}_{H} denoted by [H], helium-hydrogen mixture $\mathfrak{M}_{\text{He-H}}$ denoted by [He-H], a mixture with all species considered \mathfrak{M} in this work denoted by [all], and a 1D distribution of each ambipolar diffusion coefficient for each of these quantities at $x = 15.2$ Mm.

having a better description of the collision frequencies in solar physics MHD numerical models.

6. Conclusion

In this study, we have focused on a hydrogen–helium-ionized metals mixture. This mixture is chosen as being representative of the main composition of the solar atmosphere. However, we point out that the entire strategy of this work can be easily extended to any multicomponent plasma mixture as long as the required data for calculating the collision frequencies are provided.

By focusing on a classical 13N moment model derived by Zhdanov (2002), we have reviewed the definition of the collision frequency and the momentum and energy exchange terms in the context of a multifluid MHD model. This collision frequency is at the kinetic level derived from the Boltzmann equations and depends on so-called Chapman–Cowling collision integrals. These integrals are calculated from the integration of the transport cross section over the reduced collision velocity between the two colliding particles. The transport cross sections are determined from the integration of the impact parameter or deflection angle, which depend on a phenomenological potential that simulates the interaction between these two particles at the microscopic scale level.

In order to assess the collision frequencies for solar atmospheric conditions, we have focused on the calculation of the collision integrals based on the database provided by Bruno et al. (2010), denoted by [A1], which has been implemented in a C++ library called *Mutation++*. This database has been derived for the thermodynamic conditions associated with the Jovian atmosphere for temperatures ranging from 50 to 50,000K. In this work, we have extended this database to thermodynamic conditions representative of the solar atmosphere. The collision integrals have been extrapolated up to 4×10^5 K using the fitting expressions provided by Bruno et al. (2010). We point out that collision integral data considered for the Jovian atmosphere can be applied to any other environments, such as the solar atmosphere, for any range of densities and temperatures as long as the continuum description of the multicomponent plasma is valid. In this work, the continuum description is assumed to be valid from the photosphere to the corona. In order to make the database available, we have reviewed it and presented the methods used by Bruno et al. (2010) to calculate these collision integrals.

For all the possible interactions involved in \mathfrak{M} , we have presented the spatial variation in a 2.5 D simulation of the solar atmosphere from *Bifrost*. In addition, we have calculated the collision frequencies and compared them with the approach described by Vranjes & Krstic (2013), Vranjes et al. (2008), and Leake et al. (2012). These comparisons have been performed in four different regions representative of different layers of the solar atmosphere, ranging from the photosphere to the upper layer of the transition region. In summary, for electron–neutral interactions, the collision frequencies are similar between [A1] and [A2], leading to a ratio of the two approaches (defined by $\nu^{\text{col},[A2]}/\nu^{\text{col},[A1]}$) that ranges from 0.9 to 1.5 in all layers of the solar atmosphere. With respect to neutral–neutral interactions, in particular the H–H interaction, the ratio is high and ranges from 12 to 25. However, this interaction is not relevant for the modeling of the solar atmosphere as this interaction is not generally taken into account in a fluid MHD system of equations. Regarding ion–

neutral interactions, comparisons based on three groups have been performed. For interactions involving resonant charge transfer, in particular, the H–H⁺, the ratio ranges from 1.5 to 2.

For interactions between ionized metals and neutrals, the ratio is much higher and ranges from 200 to 600. Thus, the approximation based on the ratio of mass defined by Vranjes & Krstic (2013) should be reconsidered. In addition, for the He–H⁺ interactions, the ratio ranges from 10 to 15 in all layers of the solar atmosphere. These large differences are due to the different formalism used by Vranjes & Krstic (2013) to calculate the collision frequency. Indeed, in Vranjes & Krstic (2013), the classical formalism based on collision integrals has not been considered. Unlike in the definition of Zhdanov (2002), the momentum transport cross section is not integrated over the reduced collision velocity.

In order to quantify the impact of this formalism on the decoupling between ionized species and neutrals in the solar atmosphere, we have briefly introduced the ambipolar diffusion coefficient in the context of a single-fluid MHD model. The ambipolar diffusion has been shown to be important in the dynamics and energetics in the chromosphere (Martínez-Sykora et al. 2012, 2018; De Pontieu et al. 2017b; Martínez-Sykora et al. 2017a; Khomenko et al. 2014a, 2014b). The results from Martínez-Sykora et al. (2012) show that the ambipolar diffusion plays a major role in the formation and thermal evolution of the spicules as well as in the thermodynamics in the chromosphere, e.g., cold expanding bubbles. In addition, the ambipolar diffusion appears to have an impact on the amount of magnetic flux that can penetrate into the chromosphere from below (Martínez-Sykora et al. 2017a; Leake et al. 2014). The ambipolar diffusion coefficient depends on collision frequencies between ionized species and neutrals. For this case of ambipolar diffusion, we have also performed a detailed comparison of the differences between both approaches to calculating the collision frequencies. [A1] includes a formalism with collision integrals, while [A2] represents the formalism that has been used in the past few years in various studies. For the range of densities and temperatures representative of the solar atmosphere, our results have shown large differences, i.e., a ratio of the two ambipolar diffusion ($\eta_{\text{amb}}^{[2]}/\eta_{\text{amb}}^{[1]}$) coefficient ranging from $10^{-2.5}$ to 10^{-1} , between the two formalism. These differences are shown in the right panel of Figure 15. In general, the ambipolar diffusion coefficient calculated from our novel approach that includes collision integrals appears to be much larger than in the approach of Vranjes & Krstic (2013).

Finally, in order to assess the impact of the different ionized and neutral species interactions of \mathfrak{M} in the solar atmosphere, we have calculated the ambipolar diffusion coefficient for three different mixtures based on the approach of Vranjes & Krstic (2013) and Bruno et al. (2010): a hydrogen mixture \mathfrak{M}_{H} , a helium–hydrogen mixture $\mathfrak{M}_{\text{He-H}}$, and \mathfrak{M} . To summarize, the interactions associated with H–H⁺ and neutrals-ionized metals (in particular, Mg⁺ and Fe⁺) dominate the bottom layer of the solar atmosphere corresponding to the photosphere and bottom of the chromosphere. When helium species are considered, the ambipolar diffusion coefficient increases in upper layers, corresponding to the chromosphere and transition region. Ion–neutral interactions involving helium species appear to be the dominant interactions in these regions of the solar atmosphere. This is due to the presence of neutral helium species in the upper layer of the atmosphere. Generally, the

ratio of the ambipolar diffusion coefficients between the two approaches ranges between $10^{-2.5}$ and 10^{-1} (see Nóbrega-Siverio et al. 2020). Therefore, a significantly higher energy release due to the decoupling between ionized species and neutrals is expected. Similarly, the larger decoupling between ions and neutrals in the upper chromosphere may affect several other recent results regarding flux emergence.

To further quantify how our novel approach to calculating the collision impacts the thermodynamics of the solar atmosphere on macroscopic scales, it would be necessary to perform a numerical simulation with the two different formalisms of ambipolar diffusion coefficients and compare the results. This work is a first step for solar physics modelers toward having a complete and accurate description of the collisions in MHD numerical simulations.

We thank our colleague Prof. Magin from the Aeronautics and Aerospace Department at von Karman Institute for Fluid Dynamics in Belgium, who provided insight and expertise that greatly assisted the research.

We gratefully acknowledge support by NASA contracts, NNX17AD33G, 80NSSC18K1285, 80NSSC20K1272, and NNG09FA40C (IRIS), NSF contract AST1714955. The simulations have been run on clusters from the Notur project, and the Pleiades cluster through the computing project s1061, s2053 and s8305 from the High End Computing (HEC) division of NASA. We gratefully acknowledge the support of the Research Council of Norway through contract 230938/F50 and through grants of computing time from the Programme for Supercomputing.

Appendix A

Definition of the Interaction Potential for Coulomb Interactions

As described by Capitelli et al. (2000) and Capitelli (1977), interaction potentials associated with Coulomb or charged interactions are represented by a Coulomb potential that takes into account the Debye length (commonly called the Debye-Hückel potential) as follows:

$$\phi_{a\bar{a},a'\bar{a}'}(r) = \frac{z_{a\bar{a}}z_{a'\bar{a}'}}{r} \frac{q_e^2}{4\pi\epsilon_0} \exp\left(-\frac{r}{\lambda_D}\right), \quad (17)$$

where $z_{a\bar{a}}$ and $z_{a'\bar{a}'}$ are the elementary charges of the colliding particles, λ_D is the Debye length, and ϵ_0 is the vacuum permeability. The Debye length represents a characteristic length over which the electroneutrality assumption for charged particles is considered. When the plasma is out of thermal equilibrium, the Debye length takes into account both electron and ion temperatures as follows:

$$\lambda_D^2 = \frac{\epsilon_0 k_B / q_e^2}{n_e / T_e + \sum_{j \in \mathfrak{M}}^{j \neq e} n_j / T_j}. \quad (18)$$

In Bruno et al. (2010), ions are included in the shielding. For neutral plasma at equilibrium temperature, the Debye length

simplifies to

$$\lambda_D^2 = \frac{\epsilon_0 k_B / q_e^2}{n_e / T_e}. \quad (19)$$

Following Capitelli et al. (2000), collision integrals for Coulomb interactions are generally known either in tabular form or are approximated with closed forms of the type

$$\begin{aligned} \Omega_{a\bar{a},a'\bar{a}'}^{(1,s)}(T) &= \pi \left[\frac{4}{s(s+1)} \right] b_0^2 \left[\ln \Lambda - \frac{1}{2} - 2\tau + z(s) \right] \\ \Omega_{a\bar{a},a'\bar{a}'}^{(2,s)}(T) &= \pi \left[\frac{12}{s(s+1)} \right] b_0^2 [\ln \Lambda - 1 - 2\tau + z(s)], \end{aligned} \quad (20)$$

where $\Lambda = 2\lambda_D/b_0$ is the ratio of the Debye length and the average closest-impact parameter b_0 . Additionally, we have

$$\tau = 0.577, \quad z(s) = \sum_{n=1}^{s-1} \frac{1}{n}. \quad (21)$$

$\ln \Lambda$ is the Coulomb logarithm, which is the dominant term of Equation (20).

Appendix B

Definition of the Interaction Potential Based on a Polarization Model

The interaction potential function associated with a polarization model reads

$$\phi(r) = -\frac{z^2 q_e^2 \alpha_{\text{pol}}}{8\pi\epsilon_0 r^4} = -\frac{d}{r^4}, \quad (22)$$

where α_{pol} is the polarizability of the neutral collider, z is the elementary charge of the ion collider, and $d = z^2 q_e^2 \alpha_{\text{pol}} / 8\pi\epsilon_0$. In this framework, the collision integrals assume a closed form as follows:




$$\begin{aligned} \Omega_{a\bar{a},a'\bar{a}'}^{(l,s)}(T) &= \frac{4(l+1)}{(s+1)! [2l+1 - (-1)^l]} \\ &\times A^l (\delta = 4) \sqrt{\frac{4d}{k_B T}} \Gamma\left(s+2 - \frac{1}{2}\right), \quad a\bar{a}, a'\bar{a}' \in \mathfrak{M}^2, \end{aligned} \quad (23)$$

where Γ is the Gamma function and A^l is a coefficient correlated to the transport cross section. The latter has been computed by Smith (1967) for $l = 1, 2$ and 3 ($A^1(4) = 0.5523$, $A^2(4) = 0.3846$, and $A^3(4) = 0.6377$). These coefficients lead to simplified relations of the collision integrals. In particular, we have

$$\Omega_{a\bar{a},a'\bar{a}'}^{(1,1)}(T) = 424.443z \sqrt{\frac{\alpha_{\text{pol}}}{T}}, \quad (24)$$

where the polarizability value of H is $\alpha_{\text{pol}} = 0.6668 \text{ \AA}^3$ and He is $\alpha_{\text{pol}} = 0.205 \text{ \AA}^3$. Other polarizability coefficients for the hydrogen-helium mixture can be found in Bruno et al. (2010). The polarizability coefficients associated with any species can be found in Schwerdtfeger & Nagle (2019). Note that if we consider the definition of the collision integrals in Equation (24), the resulting collision frequency defined in Equation (4) does not depend on the temperature.

ORCID iDs

J. Martínez-Sykora  <https://orcid.org/0000-0002-0333-5717>
 V. H. Hansteen  <https://orcid.org/0000-0003-0975-6659>
 B. De Pontieu  <https://orcid.org/0000-0002-8370-952X>

References

- Alvarez Laguna, A., Lani, A., Deconinck, H., Mansour, N. N., & Poedts, S. 2016, *JCoPh*, **318**, 252
- Alves, L. L., Bartschat, K., Biagi, S. F., et al. 2013, *JPhD*, **46**, 334002
- Aubret, J., Elchinger, M. F., Rat, V., & Fauchais, P. 2003, *JPhD*, **37**, 34
- Bai, X.-N., & Stone, J. M. 2011, *ApJ*, **736**, 144
- Ballester, J. L., Alexeev, I., Collados, M., et al. 2018, *SSRv*, **214**, 58
- Bederson, B., & Kieffer, L. J. 1971, *RvMP*, **43**, 601
- Braginskii, S. I. 1965, *RvPP*, **1**, 205
- Bray, I., Kononov, D. A., & McCarthy, I. E. 1991, *PhRvA*, **43**, 5878
- Bruno, D., Catalfamo, C., Capitelli, M., et al. 2010, *PhPl*, **17**, 112315
- Capitelli, M. 1977, *JPhyC*, **38**, 227
- Capitelli, M., Gorse, C., Longo, S., & Giordano, D. 2000, *JTHT*, **14**, 259
- Carlsson, M., & Leenaarts, J. 2012, *A&A*, **539**, A39
- Chapman, S., & Cowling, T. G. 1970, *The Mathematical Theory of Non-uniform Gases. An Account of the Kinetic Theory of Viscosity, Thermal Conduction and Diffusion in Gases* (Cambridge: Cambridge Univ. Press)
- Chintzoglou, G., Pontieu, B. D., Martínez-Sykora, J., et al. 2021, *ApJ*, **906**, 83
- Cowling, T. G. 1962, *RPPH*, **25**, 244
- Daybelge, U., Kruger, C. H., & Mitchner, M. 1968, *AIAAJ*, **6**, 1712
- De Pontieu, B., De Moortel, I., Martínez-Sykora, J., & McIntosh, S. W. 2017a, *ApJL*, **845**, L18
- De Pontieu, B., Martínez-Sykora, J., & Chintzoglou, G. 2017b, *ApJL*, **849**, L7
- Devoto, R. S. 1968, *JPIPh*, **2**, 617
- Ferziger, J. H., & Kaper, H. G. 1973, *AmJPh*, **41**, 601
- González-Morales, P. A., Khomenko, E., Downes, T. P., & de Vicente, A. 2018, *A&A*, **615**, A67
- Gorse, C., & Capitelli, M. 2001, *Atomic and Plasma–Material Interaction Data for Fusion*, Vol. 9 (Vienna: IAEA), 75
- Grad, H. 1949, *Commun. Pure Appl. Math.*, **2**, 331
- Graille, B., Magin, T. E., & Massot, M. 2009, *Math. Models Methods Appl. Sci.*, **19**, 527
- Gudiksen, B. V., Carlsson, M., Hansteen, V. H., et al. 2011, *A&A*, **531**, A154
- Gupta, G. P., & Mathur, K. C. 1980, *JPhB*, **13**, 1719
- Hayek, W., Asplund, M., Carlsson, M., et al. 2010, *A&A*, **517**, A49
- Hurly, J., & Mehl, J. B. 2007, *J. Res. Natl. Inst. Stand. Technol.*, **112**, 75
- Janev, R. K., Langer, W. D., & Evans, K. J. E. P. D. 1987, *Elementary Processes in Hydrogen–Helium Plasmas* (Berlin: Springer-Verlag)
- Khomenko, E., & Collados, M. 2012, *ApJ*, **747**, 87
- Khomenko, E., Collados, M., Díaz, A., & Vitas, N. 2014a, *PhPl*, **21**, 092901
- Khomenko, E., Díaz, A., de Vicente, A., Collados, M., & Luna, M. 2014b, *A&A*, **565**, A45
- Khomenko, E., Vitas, N., Collados, M., & de Vicente, A. 2018, *A&A*, **618**, A87
- Kihara, T., Taylor, M. H., & Hirschfelder, J. O. 1960, *PhFl*, **3**, 715
- Kolesnikov, A. 2003, in *41st Aerospace Sciences Meeting and Exhibit* (Reston, VA: American Institute of Aeronautics and Astronautics), AIAA 2003-1055
- Krstic, P. S., & Schultz, D. R. 1998, *Atomic and Plasma–Material Interaction Data for Fusion*, Vol. 8 (Vienna: IAEA)
- Krstic, P. S., & Schultz, D. R. 1999, *JPhB*, **32**, 2415
- Kruger, C. H., & Mitchner, M. 1967, *PhFl*, **10**, 1953
- Kuntz, P. J., & Roach, A. C. 1972, *J. Chem. Soc., Faraday Trans.*, **2**, 259
- Leake, J. E., & Arber, T. D. 2006, *A&A*, **450**, 805
- Leake, J. E., DeVore, C. R., Thayer, J. P., et al. 2014, *SSRv*, **184**, 107
- Leake, J. E., & Linton, M. G. 2013, *ApJ*, **764**, 54
- Leake, J. E., Lukin, V. S., Linton, M. G., & Meier, E. T. 2012, *ApJ*, **760**, 109
- Li, Y., & Lin, C. D. 1999, *PhRvA*, **60**, 2009
- Magin, T., & Degrez, G. 2004a, *PhRvE*, **70**, 046412
- Magin, T. E., & Degrez, G. 2004b, *JCoPh*, **198**, 424
- Martínez-Sykora, J., De Pontieu, B., Carlsson, M., et al. 2017a, *ApJ*, **847**, 36
- Martínez-Sykora, J., De Pontieu, B., De Moortel, I., Hansteen, V. H., & Carlsson, M. 2018, *ApJ*, **860**, 116
- Martínez-Sykora, J., De Pontieu, B., & Hansteen, V. 2012, *ApJ*, **753**, 161
- Martínez-Sykora, J., De Pontieu, B., Hansteen, V. H., et al. 2017b, *Sci*, **356**, 1269
- Martínez-Sykora, J., Hansteen, V. H., Gudiksen, B., et al. 2019, *ApJ*, **878**, 40
- Martínez-Sykora, J., Leenaarts, J., De Pontieu, B., et al. 2019, *ApJ*, **889**, 95
- Martínez-Sykora, J., Rouppe van der Voort, L., Carlsson, M., et al. 2015, *ApJ*, **803**, 44
- Nóbrega-Siverio, D., Martínez-Sykora, J., Moreno-Insertis, F., & Carlsson, M. 2020, *A&A*, **638**, A79
- Ni, L., Ji, H., Murphy, N. A., & Jara-Almonte, J. 2020, *RSPSA*, **476**, 20190867
- Ni, L., & Lukin, V. S. 2018, *ApJ*, **868**, 144
- Niedziela, R., Murawski, K., & Poedts, S. 2021, *A&A*, **652**, A124
- Nóbrega-Siverio, D., Martínez-Sykora, J., Moreno-Insertis, F., & Carlsson, M. 2020, *A&A*, **633**, A66
- Olson, R. E., & Liu, B. 1980, *PhRvA*, **22**, 1389
- Oppenheim, M., Dimant, Y., Longley, W., & Fletcher, A. C. 2020, *ApJL*, **891**, L9
- Pelekhat, M., Murawski, K., & Poedts, S. 2021, *A&A*, **652**, A114
- Pirani, F., Alberti, M., Castro, A., Moix Teixidor, M., & Cappelletti, D. 2004, *CPL*, **394**, 37
- Pirani, F., Maciel, G. S., Cappelletti, D., & Aquilanti, V. 2006, *IRPC*, **25**, 165
- Popescu Braileanu, B., Lukin, V. S., Khomenko, E., & de Vicente, Á 2019, *A&A*, **627**, A25
- Rainwater, J. C., Holland, P. M., & Biolsi, L. 1982, *The Journal of Chemical Physics*, **77**, 434
- Rundel, R. D., Nitz, D. E., Smith, K. A., Geis, M. W., & Stebbings, R. F. 1979, *PhRvA*, **19**, 33
- Schwerdtfeger, P., & Nagle, J. K. 2019, *MolPh*, **117**, 1200
- Scoggins, J. B., Knisely, C. P., & Magin, T. E. 2016, in *AIP Conf. Proc. 1786, 30th Int. Symp. on Rarefied Gas Dynamics*, ed. A. Ketsdever & H. Struchtrup (Melville, NY: AIP), 130002
- Smith, F. J. 1967, *High order collision integrals*, Final Report NSR 52-112-00, NASA
- Spitzer, L. 1963, *AmJPh*, **31**, 890
- Stallcop, J. R., Levin, E., & Partridge, H. 1998, *JTHT*, **12**, 514
- Stallcop, J. R., Partridge, H., & Levin, E. 1996, *CPL*, **254**, 25
- Struchtrup, H. 2005, *Macroscopic Transport Equations for Rarefied Gas Flows—Approximation Methods in Kinetic Theory* (Berlin: Springer) **10**, 1007/3-540-32386-4
- Vernazza, J. E., Avrett, E. H., & Loeser, R. 1981, *ApJS*, **45**, 635
- Vranjes, J., & Krstic, P. S. 2013, *A&A*, **554**, A22
- Vranjes, J., Poedts, S., Pandey, B. P., & De Pontieu, B. 2008, *A&A*, **478**, 553
- Wargnier, A. L. A., Scoggins, J. B., et al. 2020, *A&A*, **635**, A87
- Wójcik, D., Kuźma, B., Murawski, K., & Musielak, Z. E. 2020, *A&A*, **635**, A28
- Woods, L. C. 1995, *JFM*, **286**, 406
- Zhdanov, V. 2002, *PPCF*, **44**, 2283